1. INTRODUCTION

The elastic scattering of electrons by neutrons and protons provided direct experimental evidence for the compositeness of hadrons (1). Appropriately, subsequent deep inelastic experiments using lepton beams revealed that hadrons are composed of point-like constituents whose properties are identical with those of quarks, the fundamental hadronic states representing the SU(3) algebra. The quark model had been successful in describing masses and magnetic moments of hadrons (2). The use of high energy leptons as probes of nucleon structure is unique because the leptons do not interact strongly, so that they are able to penetrate the nuclear surface; their short wavelength implies that the leptons collide with individual charged or weakly interacting constituents.

About twenty years ago, systematic measurements (3) were begun of the inelastic reaction in which the nucleon, N, does not remain intact:

$$e^- + N \rightarrow e^- + X, \qquad 1.$$

where X is some ensemble of hadrons. These experiments gave larger cross sections than had been anticipated and manifested some surprising regularities that were dubbed "scaling" (4). A consistent and attractive interpretation emerged in which the scattering occurred between the lepton and one of the fundamental constituents, or "partons," of the nucleon (5). A short time later, charged-current neutrino experiments (6),

$$\nu_\mu + N \rightarrow \mu^- + X, \qquad 2.$$

were interpreted in the same way.

This model interpretation of deep inelastic scattering has led to two decades of experimentation using all available leptonic probes: electrons (e^-), muons (μ^-), and neutrino (ν), along with their antiparticles. (Several experimental methods are described in Section 2.) The scattering of leptons from nucleon targets cleanly delineates the properties of those parton constituents containing electric or weak charge. In the last decade, with the advent of an attractive theory of the strong interactions, quantum chromodynamics (QCD) (7), deep inelastic data have provided important contact with experiment; in the process, measurements have been made of the dimensionless coupling (α_s) between quarks and gluons, a fundamental parameter of QCD.

Understanding nucleon structure has been important; however, deep inelastic scattering has contributed to our understanding in other ways. Neutral-current phenomena, which provided the first demonstration of the SU(2) × U(1) unification of weak and electromagnetic interactions

(8), were discovered (9) and corroborated (10) in neutrino-nucleon experiments; interference between neutral weak and electromagnetic propagators was demonstrated first in an electron-nucleon inelastic scattering experiment (11). To date, the most precise measurement of the "weak mixing" or "Weinberg" angle, θ_W, parametrizing weak neutral-current coupling, comes from neutrino-nucleon data. (The advent of precise measurements at Z^0 factories should soon change this.) The electroweak theory, together with the quark hypothesis and QCD, forms the basis for the "standard model" of elementary particles. For reasons of brevity and because good reviews exist (12a,b,c), we do not discuss neutral-current measurements in this review except insofar as they relate to nucleon structure.

Deep inelastic scattering has been a fertile ground for searching out new phenomena. For example, there had been indications of anomalous behavior in the neutrino production of like-sign dimuon events, which we address below. In addition, experiments have ruled out important regions of parameter space for existence of neutral massive leptons. A short summary of the status of these and other searches for exotic phenomena is included in Section 5.

1.1 *Formalism of Deep Inelastic Scattering*

The description of events in deep inelastic scattering relies on three important event parameters: the square of the center-of-mass energy, s, and the scaling parameters, x and y. The scaling parameters provide a simple intuitive picture of the scattering between lepton and parton. The meaning of the x parameter is pictured in Figure 1: in a Lorentz frame in which the

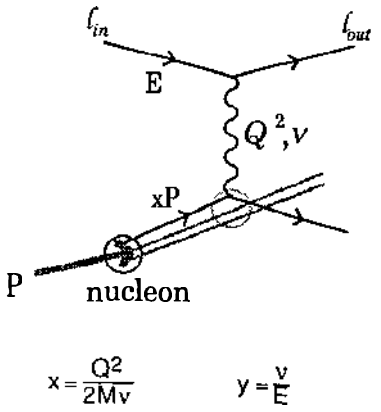

ℓ_{in}	ℓ_{out}	
$\mu^{\pm}$	$\mu^{\pm}$	}electromagnetism (EM)
$e^{\pm}$	$e^{\pm}$	
ν_μ	μ^-	}Weak (CC)
$\bar{\nu}_\mu$	μ^+	
ν_μ	ν_μ	}Weak (NC)
$\bar{\nu}_\mu$	$\bar{\nu}_\mu$	

Figure 1 Deep inelastic scattering of nucleons by leptons.

nucleon is traveling at high momentum, P, the struck parton carries momentum, xP. The y variable is directly related to the two-body scattering angle, θ^*, of the outgoing lepton in the center-of-mass frame of the initial-state lepton and the struck parton: $\cos\theta^* = (1+y)/2$. The interesting point is that these and other parameters of the event can be calculated from a few measurable laboratory quantities:

E = incident beam lepton energy,

E' = outgoing lepton energy,

θ = outgoing lepton angle with respect to the beam direction, and

ν = outgoing hadronic energy.

For a discussion of the relationship between the scaling parameters and experimentally measured quantities, see for example (13) and references quoted there. The parameters noted here are relevant to the fixed-target experiments. For the ep collider case, see (16).

Specifically, the deep inelastic parameters depend on the energy, but not on other details of the hadronic final state. Conservation of energy constrains E, E', and ν. Unless otherwise stated, all masses are assumed small, including the nucleon mass (M), in comparison to the momentum transfer between the lepton and participating parton. The momentum transfers in present fixed-target experiments are small in comparison to the mediating weak boson masses, so effects of those masses are ignored in the formulae that follow.

The overall center-of-mass energy between lepton and nucleon is

$$s = 2ME.$$

The four-momentum transfer between lepton and nucleon vertices, q_μ, has a magnitude determined directly from measurements of the initial and final leptons:

$$-q^2 = Q^2 = 2EE'(1-\cos\theta) \simeq EE'\theta^2.$$

The dimensionless scaling variables, x and y, are calculated from the measured quantities as follows:

$$x = Q^2/2M\nu \qquad y = \nu/E.$$

These follow (13) from the more general Lorentz-invariant relations,

$$x = Q^2/2P\cdot q \qquad y = 2P\cdot q/s.$$

1.2 *Structure Functions and Cross Sections*

Individual events are characterized by unique values of x, y, and Q^2; accumulation of many such events permits measurement of the differential cross sections with respect to two of these variables. Cross sections are commonly parametrized in terms of structure functions, which are related by the quark model to the densities of partons within the nucleon (see Section 1.3). We illustrate this for the fixed-target scattering of leptons with nucleons.

Consider the differential cross section for the νN charged-current scattering (Reaction 2, above),

$$\frac{d^2\sigma^{\nu N}}{dx\,dy} = \frac{G^2 ME}{\pi}\{F_2^{\nu N}(x,Q^2)[1-y] + 2xF_1^{\nu N}(x,Q^2)[y^2/2] + xF_3^{\nu N}(x,Q^2)\,y[1-(y/2)]\}, \quad 3.$$

in terms of the three structure functions: F_2, $2xF_1$, and xF_3. The y dependence (or $\cos\theta^*$ dependence) is a consequence of the helicity structure of the weak current. The function, xF_3, measures the parity-violating part of the cross section. The analogous expression for muon or electron scattering from nucleons (Reaction 1) may be obtained by making the following formal replacements in Equation 3:

$$G^2/\pi \to 8\pi\alpha^2/Q^4;$$

$$F_2^{\nu N}(x,Q^2) \to F_2^{\mu N}(x,Q^2);$$

$$xF_1^{\nu N}(x,Q^2) \to xF_1^{\mu N}(x,Q^2);$$

$$xF_3^{\nu N}(x,Q^2) \to 0. \quad 4.$$

The function xF_3 is absent since muon scattering is dominated by parity-conserving photon exchange at momentum transfers typical of fixed-target experiments.

The historical fact is that the structure functions, while strongly dependent on x, were seen to be largely independent (at the $\pm 10\%$ level) of the momentum transfer variable, Q^2, when x is fixed. This independence of Q^2 is the quantitative statement of scaling (4). It led to the physical interpretation that the nucleon consisted of nearly free partons and that the structure functions were the momentum densities (or squared wave functions) of partons within a nucleon (5). The deviations from scaling could be attributed to the potential and kinetic energies of these partons: scaling deviations are now expected to be understandable as consequences

of the strong QCD binding forces. It follows that certain features of the structure functions are predictable within the context of perturbative QCD (see Section 2.5).

Another important historical point, evident from the earliest experiments, was that $F_2(x) \approx 2xF_1(x)$ (the Callan-Gross relation). The small value (less than about 0.2) of

$$R = (F_2 - 2xF_1)/2xF_1 \qquad 5.$$

was recognized (14) to be a consequence of the nearly free spin-1/2 constituents dominating the scattering process. Again, deviations from zero are expected and predictable at high Q^2 by perturbative QCD. We return to these important questions of deviations from exact scaling and finite R values below.

1.3 *Parton Densities and Structure Functions*

Within the context of the quark model, the compositeness of any hadron can be described by the densities of its constituent quarks. For example, the function $u(x)\,dx$ specifies the differential probability for finding a u quark in a proton carrying a fraction between x and $x+dx$ of the proton momentum. Knowledge of the quark and antiquark densities [denoted generically $q(x)$ and $\bar{q}(x)$, respectively] is of considerable importance in making reliable estimates of parton luminosities for collider experiments; indeed, it is the limiting factor in constraints on the number of neutrino generations and on the mass of the top quark that can be obtained from present measurements using hadron colliders (15). Furthermore, quark densities are important in predicting the standard model behavior of the cross section at HERA, where the Q^2 and x range will be extended by two orders of magnitude (16).

A complete theory of nucleon constituents and of the strong interactions would permit us, at least in principle, to predict parton densities for any hadron. This ability eludes us at present. Nevertheless, QCD allows us to evolve densities from one energy to another. Furthermore, the quark model does permit us to calculate structure functions for any deep inelastic process directly from parton densities. [For a detailed recipe of structure functions in terms of parton densities, see for example the review by Fisk & Sciulli (13).] Conversely, measured structure functions permit extraction of parton densities. In Section 3 we discuss the extracted densities for u and d quarks inside the nucleon from proton and neutron structure functions. The overall isoscalar quark and antiquark densities, which are more precisely known, are also discussed. Comparison of structure functions measured with differing nuclear targets allows us to determine how the nuclear environment influences the parton densities.

We also discuss in Section 3 measurements of the density of strange quarks from ν_μ-induced events with two opposite-sign muons in the final state. These events arise mainly from the charged-current production and semileptonic decay of charm, which is preferentially produced from strange quarks.

The use of polarized muons with polarized hydrogen targets permits measurements of the cross sections with muon and proton spin aligned and opposite. Such asymmetries measure the "spin-dependent structure function," $xg_1^p(x)$ (see Equation 10).

One important qualitative distinction between the weak and electromagnetic interactions in Reactions 2 and 1, respectively, is that the scattering by neutrinos depends on x times the density of quarks inside the nucleon, while the scattering by electrons or muons depends on the square of the quark electric charge as well. The sum of the neutrino and antineutrino total cross sections is proportional to the integrals of the structure functions and provides a measure of the fraction of the proton momentum carried by struck quarks. Early measurements of these cross sections, at both low (18) and high (19) energies, demonstrated that only about half the nucleon momentum is carried by quarks. This provided a direct indication that hadrons carried fundamental quanta in addition to quarks; the missing momentum is known to be carried by gluons (20). The ratio of muon to neutrino scattering, on the other hand, measures the mean-square charge of quarks, as discussed below.

The quark model inherently provides beautiful relationships among structure functions measured by different inelastic processes; it further permits predictions about certain properties of those structure functions. Some of the simplest predictions and best experimental tests involve isoscalar nucleon targets, containing equal numbers of u and d quarks. The measurements, accomplished with heavy nuclear targets to provide high rate, sometimes require small corrections for neutron excess. The following quark model predictions for isoscalar targets can be tested:

1. The ratio of the F_2 structure functions for muon (or electron) to neutrino scattering is the mean-square quark charge in units of the square of the electron charge. That is,

$$\frac{F_2^{\mu N}(x)}{F_2^{\nu N}(x)} = \frac{5}{18}\left(1 - \frac{3}{5}\frac{s+\bar{s}}{q+\bar{q}}\right), \qquad 6.$$

where the small x-dependent correction is due to the asymmetric number of strange and charm quarks in the nucleon.

2. Structure functions obtained with neutral-current interactions ($\nu_\mu + N \rightarrow \nu_\mu + X$) are directly predictable from those obtained with charged-

current interactions. Measurements of neutral-current structure functions are much more difficult since both the initial- and final-state leptons are neutral. This is discussed in Section 3.1.

3. Certain of the sum rule predictions, described in the next section, can be tested.

1.4 *Sum Rules*

Sum rule predictions were originally obtained using rigorous current algebra formulations, but they can also be obtained from a naive non-relativistic quark model, which we describe here for pedagogical reasons. The relevant quantities are obtained by integrating appropriate measured structure functions weighted by $1/x$. These integrals are then directly related to

N_u = number of valence u quarks inside the proton;

N_d = number of valence d quarks inside the proton;

e_u = charge of u quark; and

e_d = charge of d quark.

The quark model of the proton predicts $N_u = 2$ and $N_d = 1$; $e_u = +2/3$ and $e_d = -1/3$. The comparison with data is discussed in Section 3. We mention here several specific sum rules.

1. The Gross–Llewellyn Smith (GLS) sum rule is the best known because it is the best tested (21). It states (22)

$$S_{GLS} \equiv \int_0^1 \frac{xF_3^{\nu N}}{x}\,dx = (N_u + N_d)\left(1 - \frac{\alpha_s}{\pi}\right). \qquad 7.$$

This relation is a consequence of the fact that the parity-violating structure function, in the quark model, is equal to the difference between the quark and antiquark densities, which is just the valence quark density. An experimental value for S_{GLS} near 3 corroborates, then, that the partons defining the nucleon quantum numbers carry baryon number 1/3. The presence of the term with α_s illustrates that some sum rules should have perturbative QCD corrections, like GLS, while others, like the Adler sum rule, do not.

2. Adler (23) sum rule: This integral can be obtained from neutrino data using hydrogen and deuterium targets:

$$S_A \equiv \frac{1}{2}\int_0^1 \frac{dx}{x}(F_2^{\nu p} - F_2^{\bar{\nu} p}) \cdots (N_u - N_d), \qquad 8.$$

which is unity for quark constituents.

3. Gottfried (24) sum rule: This integral is obtained using muon or electron data from hydrogen and deuterium targets:

$$S_G = \int_0^1 \frac{dx}{x}(F_2^{\mu n} - F_2^{\mu p}) = (N_u - N_d)(e_u^2 - e_d^2), \qquad 9.$$

which gives 1/3 for quark constituents.

4. Bjorken (25) sum rule: The spin structure functions from proton and neutron targets are expected to satisfy

$$\int_0^1 [g_1^n(x) - g_1^p(x)]\,dx = \frac{1}{2}[(N_u^\uparrow - N_u^\downarrow) - (N_d^\uparrow - N_d^\downarrow)](e_u^2 - e_d^2)\left(1 - \frac{\alpha_s}{\pi}\right), \qquad 10.$$

where $N^\uparrow$ ($N^\downarrow$) refers to quarks with their spins parallel (antiparallel) to the spin of the nucleon. In the nonrelativistic quark model, the asymmetry of spin-oriented up and down quarks, which appears in brackets on the right-hand side of Equation 10, is equal to the expectation value of the longitudinal spinor and this is just the ratio of axial vector to vector weak couplings. That is $\langle \sigma_z \rangle = G_A/G_V$ (26; see also 25).

The predictions of these important sum rules (Equations 7–10) are discussed at length, together with comparisons with contemporary experimental results, in Section 4. To reiterate, the specific predictions quoted there are consequences of current algebra, and as such are firm predictions of the standard model.

1.5 *Quantum Chromodynamics*

QCD has been described as a "radically conservative" theory: it results from extrapolating general principles like locality, causality, and renormalizability, reconciling these with experimental fact, and accepting the conclusions that "fall short of actual contradictions" (27). It serves as a paradigm for the description of strong interactions in the same way that electromagnetic theory does for electricity. But, unlike the case for quantum electrodynamics (QED), we are severely limited in testing the predictions of QCD. One important difference is that QED becomes simple where experiments are easiest: at low momentum transfers; for QCD, the simpler predictions occur at the highest momentum transfers.

The "best" way of checking QCD, and measuring the coupling strength of quarks to gluons, is a subject of some controversy because of uncalculable contributions from "nonperturbative" effects. While there are important predictions for other processes (28), elegant and unambiguous predictions do exist for the behavior of deep inelastic structure functions. The dependence (29) of structure functions on Q^2 at fixed x and the dependence (30) of R on x and Q^2 are the most important.

Perturbative QCD only describes the evolution of structure functions (i.e. the Q^2 dependence) at collision energies where the bound kinetic and potential energies of the struck quark may be neglected. Such "higher twist" effects may be estimated but they cannot be reliably calculated because they are related to unknown bound-state quark wave functions. From simple dimensional considerations, such terms must behave as

$$\text{higher twist terms} \approx \left(\frac{A(x)}{Q^2}\right)^n, \qquad n \geq 1, \qquad 11.$$

where the numerator, while a function of x, is presumably of the order of the size of the bound state ($A \leq 1$ GeV^2).

The diagrams contributing to the leading-order perturbative QCD corrections are shown in Figure 2, in which effects arise either because the bound quark can emit a gluon (Figure 2, *left*) or because a gluon within the nucleon can produce a quark-antiquark pair (Figure 2, *right*). In both cases, the magnitude of the effect depends on the quark-gluon coupling constant, α_s, which in leading order may be written

$$\alpha_s(Q^2) = \frac{12\pi}{(33-2N_f)\ln(Q^2/\Lambda^2)}, \qquad 12.$$

where N_f is the number of quark flavors.

R-PARAMETER If a beam lepton were to interact with a free fermion, at rest or moving collinear with the beam, the R parameter would be identically zero. As described above, effects due to the wave functions of bound quarks would create a functional dependence like that of Equation 11. If this were the complete description, the value of R would fall to zero very soon after we pass momentum transfers characteristic of soft hadronic processes. QCD, on the other hand, predicts (30) that diagrams like those in Figure 2 will contribute with the logarithmic Q^2 dependence characteristic of α_s:

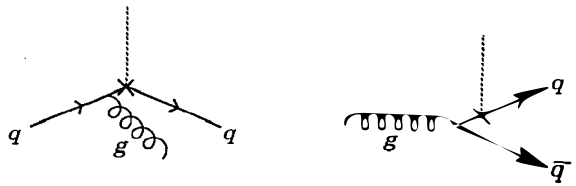

Figure 2 (*Left*) Gluon bremsstrahlung by a quark. (*Right*) Quark-antiquark pair production by a gluon. The dotted line represents the intermediate boson ($\gamma/W^{\pm}/Z^0$) coupling to the interacting quark. The coupling strength at the quark-gluon vertex is α_s.

$$R(x,Q^2)=\frac{\alpha_s(Q^2)}{2\pi}x_2\int_x^1\frac{dz}{z^3}\left[\frac{8}{3}F_2(z,Q^2)+4f\left(1-\frac{x}{z}\right)zG(z,Q^2)\right]\Big/2xF_1. \qquad 13.$$

Here f is the number of flavors (N_f) for the neutrino case, and the sum over the quark charges (Σe_i^2) for the muon or electron case. (The resulting predicted value of R is the same.) The first and second terms inside the integral correspond to contributions represented in Figures 2*a* and 2*b*, respectively. Since α_s (Equation 12) falls only logarithmically with Q^2, the value of R at fixed x should fall slowly with Q^2, so long as the momentum transfers are high enough.

STRUCTURE FUNCTION EVOLUTION Structure functions are of two types:

1. The leading-order evolution of a "nonsinglet" structure function, $F^{NS}(x,Q^2)$, is determined completely by the interaction represented in Figure 2*a*. Here the rate of change at fixed x depends directly on an integral over the same structure function (29)

$$\frac{dF^{NS}(x,Q^2)}{d\ln(Q^2)}=\frac{\alpha_s(Q^2)}{2\pi}\int_x^1 F^{NS}(z,Q^2)P_{qq}\left(\frac{x}{z}\right)dz \qquad 14.$$

and is therefore particularly simple. Here, P_{qq} is a "splitting function" determined in perturbative QCD. The xF_3 structure function and the function $F_2^n-F_2^p$ are examples of nonsinglet structure functions.

2. Singlet structure functions satisfy considerably more complicated evolution equations (29) because the Q^2 evolution has additional contributions from the process represented in Figure 2*b*. Equation 14 is modified by an additional integral on the right-hand side that depends on the gluon structure function. The gluon structure function itself satisfies a separate evolution equation dependent on two integrals. We discuss these further in Section 4.

2. DEEP INELASTIC SCATTERING EXPERIMENTS

2.1 *SLAC eN Experiments*

The program of fixed-target electron-nucleon inelastic scattering at SLAC (31) has been in operation for over twenty years. The Stanford Linear Accelerator has delivered a beam within the range 4.5–20 GeV to experiments with various targets. The scattered electron is momentum reconstructed in one of the two magnetic spectrometers; these devices, a powerful complex of detection equipment and computers, were a standard for later large detector systems.

The upstream of the two spectrometers can measure particle momenta

up to 8 GeV; the downstream device operates, with smaller solid-angle acceptance, up to 20 GeV. The energy (E) of the incident electron, as well as the energy (E') and the angle (θ) of the scattered electron, is measured with good resolution. The spectrometers employ scintillation counter hodoscopes, gas Čerenkov counters, and electromagnetic shower detectors. Charged pions and electrons arising from neutral pions are backgrounds for the scattered electron, particularly at low E'. Techniques for flux determination using Faraday cups and redundant monitors are well established; measurements to better than the 1% level are standard. The limit in normalization precision is typically dependent on knowledge of the spectrometer acceptance.

2.2 *Experiments with μ Beams*

Experiments utilizing muons[1] extend the eN program to higher energies ($20 < E < 300$ GeV) using beams of (polarized) muons from pion decay. The experiments enjoy much less beam flux than that at SLAC, but compensate by using detectors with large acceptance. Normalization is obtained by counting the beam particles. Programs have been operated at Fermi National Accelerator Laboratory (FNAL) (BFP collaboration) and at CERN (EMC and BCDMS collaborations). For measurements on iron, the BFP and EMC collaborations use a calorimeter as target, which provides a measure of the hadron energy (ν), while the BCDMS experiment does not. We further compare differences in technique in Section 4.

2.3 *Experiments with ν Beams*

Neutrinos, because they permit measurement of the nonsinglet (parity-violating) structure functions (xF_3), are unique probes. Studies have been carried out by collaborations using bubble chambers[2] and electronic detectors.[3] The best statistical precision on heavy materials (isoscalar targets) is available from the electronic detectors, but the bubble chamber experiments have carried out more extensive studies on hydrogen and deuterium targets. In a neutrino-induced charged-current event, the directly measured quantities are the energy transferred to the hadronic system (ν), the final-state muon energy (E'), and the muon scattering angle (θ).

[1] The major collaborations are Berkeley-Fermilab-Princeton (BFP) (32a), European Muon Collaboration (EMC) (32b,c), and Bologna-CERN-Dubna-Munich-Saclay (BCDMS) (33a,b,c).

[2] The CERN Gargamelle and BEBC programs, and the FNAL 15-foot bubble chamber programs, are described in (13).

[3] The CERN-Dortmund-Heidelberg-Saclay (CDHS) collaboration (34a), Chicago-Columbia-Fermilab-Rochester (CCFR) collaboration, the FMMF group (34b), and the CHARM collaboration (35).

Two types of high energy ν beams are commonly employed: narrow band beams and wide band beams [for a review of neutrino beam types, see (13)]. The narrow band beam provides an independent measurement of the incident neutrino energy, E. Furthermore, the beam is either almost purely neutrino or almost purely antineutrino, with little cross contamination. Normalized cross sections are most easily obtained because the flux of the parent pions and kaons is directly measured (36). Wide band beams, created by focusing with pulsed horns or with quadrupole triplets, provide an order of magnitude more neutrinos; however, there is no direct check on the event neutrino energy and no direct measure of the flux.

Since neutrino flux cannot be measured directly in wide band beams, alternative techniques for normalization must be used. Such techniques have been developed (37); they allow measures of relative normalization among the several neutrino energies, as well as the relative flux between neutrinos and antineutrinos. (The overall cross-section normalization must still be obtained from narrow band or other measurements.) These relative flux measurements, calculated directly from the events, are more precise than those that can presently be measured in more direct ways.

2.4 *HERA Collider eN Experiments*

The technology of colliding beams permits the extension of deep inelastic scattering experiments to much higher momentum transfers. This will indeed happen in the early 1990s with the commissioning of the HERA electron-nucleon collider at the DESY laboratory in Hamburg, West Germany (38). The machine utilizes counter-rotating beams of 30-GeV electrons and 820-GeV protons to achieve a center-of-mass energy (314 GeV) an order of magnitude higher than achievable with present fixed-target beams. Figure 3 shows the range in $1/x$ versus Q^2 probed by several accelerators; leptonic probes at high Q^2 and very small x will uniquely characterize the "soft" region of the nucleon (39; also W.-K. Tung, private communication).

The HERA facility will provide substantial capability for finding exotic particles and interactions (e.g. 40). Some, like certain kinds of massive, strongly interacting particles with lepton number, will be uniquely accessible. Others, such as supersymmetric particles, will have complementary searches performed at other colliding facilities and HERA. The facility will permit measurements of nucleon structure to be extended by about two orders of magnitude in Q^2 and in $1/x$ (see Figure 3). The typical momentum transfers at HERA can be comparable to the masses of the exchanged weak bosons.

HERA will be a unique laboratory for certain tests of the standard

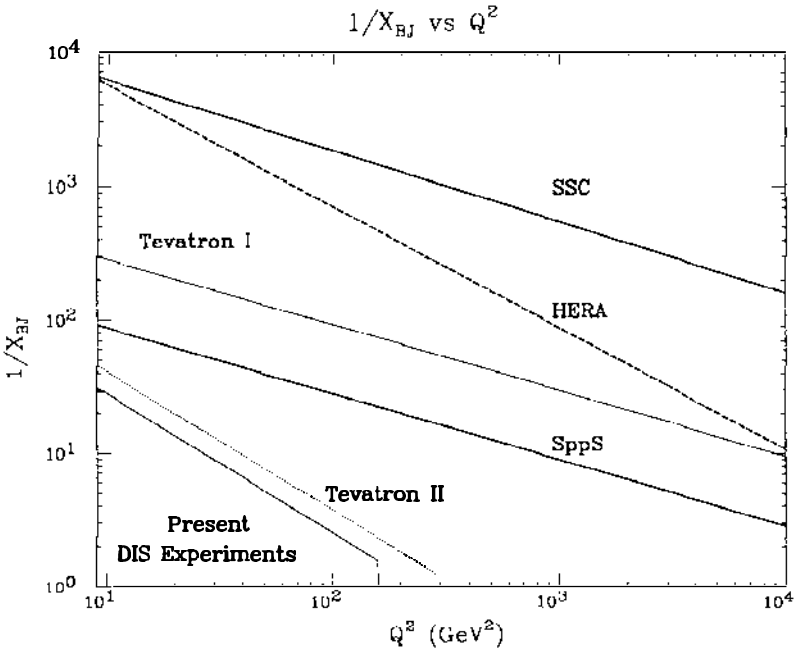

Figure 3 The $x(= X_{BJ})$ and Q^2 ranges probed by interactions at various accelerators.

model, particularly sensitive to the existence of nucleon and/or lepton substructure. Typically such structure is parametrized as a point-like four-fermion interaction conserving helicity and flavor with effective weak coupling reduced by a scale parameter, $\Lambda_{\pm}$; this contribution is assumed to interfere either positively or negatively, respectively, with the ordinary electroweak coupling. With unpolarized beams, the anticipated sensitivities extend to about $\Lambda_{\pm} \approx 4$–7 TeV, depending on the form of the coupling (41).

The accelerator is expected to provide a transversely polarized electron beam whose spin can be rotated either parallel or antiparallel to the beam direction in the intersection regions. Polarization will provide an important tool for understanding the spin dependence of known or new interactions; its use should extend the sensitivity to $\Lambda_{\pm}$ by approximately 1 to 1.5 TeV (41). In general, the ability to vary the flavor ($e^{\pm}$) and the polarization of the lepton will provide a unique parameter space for exploiting the lepton-nucleon interaction.

HERA is designed to provide a luminosity of 1.5×10^{31} cm^2 s^{-1}, or about one inverse picobarn per day. This high value, necessary so that structure functions can be measured with adequate event rates, will necessi-

tate high average proton beam currents contained in 200 stored bunches. The short time interval between beam bunches (96 ns) creates new problems for the readout and triggering electronics in an adverse radiation environment. Such technical problems are the forerunners of even more severe problems to be faced with hadron colliders (like SSC and LHC) planned for even higher energies and luminosities.

For neutral-current reactions, the direction and energy of the outgoing electron will provide measurements of the appropriate event parameters (Q^2, x, y). However, in the charged-current process

$$e + p \rightarrow \nu_e + X,$$

only the system of hadronic debris (X) is observable. The jet of hadrons that follows the direction of the outgoing parton must be used to reconstruct the event parameters. For this reason, experiments at HERA have paid close attention to designing apparatus that can reconstruct the global properties (energy and angle) of hadronic jets.

Of crucial importance in reconstructing the event parameters is the jet energy measurement. The ZEUS experiment, in response to this challenge, has opted to build a 4π compensating calorimeter, using depleted uranium and scintillator. The detector, now under construction, has a measured hadronic resolution of $\delta E/E \approx 0.35/\sqrt{E(\text{GeV})}$.

3. QUARK-PARTON MODEL: TESTS AND SUM RULES

3.1 *Universality on Isoscalar Targets by $\gamma/W^{\pm}/Z^0$ Exchange*

The structure functions that parametrize the deep inelastic cross sections are uniquely related to the nucleon quark densities. An essential element of the quark-parton picture is the universality of quark densities whether they are measured in electromagnetic, ν charged-current, or ν neutral-current interactions. For example, in μ (or e) scattering from an isoscalar target, the structure function $F_2^{\mu N}(x, Q^2)$ is proportional to the square of the electric charges and momentum densities of the interacting partons, and can be expressed (neglecting R) as

$$F_2^{\mu N}(x, Q^2) = \sum_i e_i^2 [x q_i(x, Q^2) + x \bar{q}_i(x, Q^2)], \qquad 15.$$

where the sum extends over the densities of all quark (q) and antiquark ($\bar{q}$) types and e_i is the electric charge (in units of the electron charge).

For charged-current ν scattering from an isoscalar target, the structure function $F_2^{\nu N}(x, Q^2)$ is obtained by the replacement $e_i \rightarrow 1$; while

$xF_3^{\nu N}(x, Q^2)$ is simply the appropriate difference between the quark and antiquark densities $(xq_i - x\bar{q}_i)$.

The corresponding expressions for neutral-current structure functions are obtained by the formal replacement of e_i^2 by a (known) combination of left- and right-handed coupling constants (42). These, in turn, are parametrized in terms of the usual standard model neutral-current couplings, $\sin^2 \theta_W$ and ρ, where θ_W is the Weinberg angle (12a,b,c).

NEUTRAL-CURRENT STRUCTURE FUNCTIONS Measurements of the total neutrino and antineutrino neutral-current cross sections are used to measure θ_W and ρ. The standard model, with appropriate electroweak radiative corrections, predicts the value of ρ and requires that θ_W be independent of the process. The ratio of the total neutral-current cross section to the total charged-current cross section in deep inelastic experiments provides a sensitive measure of both ρ and $\sin^2 \theta_W$. These measurements have been reviewed by others (12a,b,c), who have concluded that the deep inelastic value for ρ is in good agreement with the standard model prediction. An average from several deep inelastic measurements gives a value for $\sin^2 \theta_W$ in good agreement with the average of measurements from the vector boson masses. Other methods for measuring these parameters are not as precise, but are generally in agreement. It should be noted that the principal limitation in the deep inelastic measurement of the Weinberg angle is the uncertainty in the threshold behavior of the production of charm from down and strange quarks.

A more directed test of the quark model comprises measuring (with neutrinos) the x-dependent neutral-current structure functions and comparing them to the structure functions predicted from quark densities measured in electromagnetic and charged-current deep inelastic experiments. The measurement of these structure functions is inherently difficult because the measurement of the value of x in an individual event is imprecise: neutral-current interactions have a neutrino in the final state, and so the event parameters must come from measurements of the hadronic jet. The FMM (43a, 43b) and CHARM (44) collaborations have reported neutral-current structure functions with a typical resolution on x of about 20%. These data demonstrate good agreement between quark densities extracted from neutral-current interactions and those extracted from charged-current and electromagnetic interactions.

MEAN-SQUARE CHARGE TEST The probe independence of the parton densities requires that the ratio $F_2^{\mu N}/F_2^{\nu N}$ be nearly equal to the mean-square charge (5/18) of the quarks, as expressed in Equation 6. This is most accurately tested with high statistics data from experiments employing heavy isoscalar targets. Figure 4 shows a comparison of four data sets

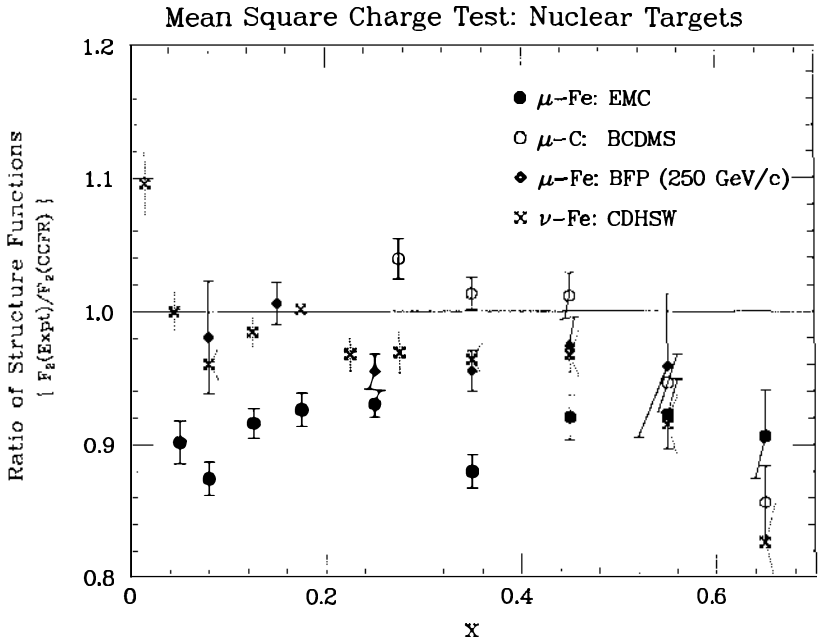

Figure 4 Ratios of F_2 measurements among two sets of neutrino experiments [CDHSW (46) and CCFR (45)] and three sets of muon experiments [BCDMS (33b), BFP (32a), and EMC (32c)]. The muon experiments have been corrected by the quark charges, so that a ratio of unity implies a mean-square charge of 5/18. All ratios are shown with respect to the CCFR data. The assumption $R = R_{QCD}$ is made with the exception of the BFP data, where $R = 0$. Small corrections for the neutron-proton excess and for the strange-charm asymmetry are included in the comparison.

[CDHSW (46), BCDMS (33b), EMC (32c), and BFP (32a)] relative to the CCFR (45) neutrino data.[4] The reported values of F_2 were interpolated or extrapolated for each x value to the mean Q^2 of the CCFR data (32a, 32c, 33b, 45, 46). The comparison of the ratios, averaged over x, of F_2 measured by several experiments relative to the CCFR experiment is presented in Table 1.

The two sets of neutrino data are in good overall agreement, although the CCFR data are somewhat different from those of CHDSW at extreme values of x where the comparison is particularly sensitive to the Q^2 extra-

[4] The data were corrected using $R = R_{QCD}$, except for BFP where $R = 0$ was assumed by the authors. Other small corrections, including the effects of neutron-proton excess in the iron target data and the effect of the strange-charm asymmetry have also been applied. See (45) for details.

Table 1 Ratio, r^{exp}, of F_2^{exp} with respect to F_2^{CCFR}

r^{CDHSW}	r^{EMC}	r^{BFP}	r^{BCDMS}
0.988	0.905	0.958	0.989

polation. These data agree within the quoted systematic normalization error of each experiment ($\sim$3%). There now exists a consistency among neutrino experiments that was lacking a few years ago (47) when newer CDHSW measurements came into agreement with those of CCFRR.

The EMC (BFP) data are 10% (4%) lower than those of the CCFR on average, but do not exhibit any appreciable x dependence. The disagreement of the EMC data average with both neutrino and other muon data is somewhat outside the quoted 5% systematic errors. While the average level of the BCDMS data shown in Table 1 is in agreement with that of the neutrino experiments, the figure does exhibit some x dependence. It should be noted that the BCDMS data are reported for $Q^2 > 30$ GeV^2, which results in a higher mean Q^2 than other experiments and consequently these data undergo larger extrapolation; this seems, however, inadequate to explain the discrepancy among the muon experiments. (A similar conclusion is reached in the comparison of the EMC hydrogen data with that of BCDMS discussed in Section 3.3.)

Thus, the mean-square charge of the quarks is measured to be 5/18, within the 5–10% differences appearing among the muon experiments. This disagreement of normalization and shape among muon experiments should be considered a problem.

3.2 *Sum Rules*

GROSS–LLEWELLYN SMITH SUM RULE The Gross–Llewellyn Smith sum rule, the most accurately tested of the sum rules, measures the number of valence quarks in the nucleon. Equation 7, with corrections due to finite Q^2, may be written

$$S_{GLS} \equiv \int_0^1 \frac{dx}{x} xF_3(x,Q^2) = 3\left[1 - \frac{\alpha_s(Q^2)}{\pi} - \frac{4}{27}\frac{\langle G_1\rangle}{Q^2} + O(Q^{-4})\right], \quad 16.$$

where the second term in the brackets corresponds to the known leading-order perturbative QCD correction and the third term, an estimate of higher twist contribution (48), is expected to be small here. The sum rule therefore predicts, using $\Lambda = 186 \pm 60$ MeV and including only the first-order perturbative QCD correction, at $Q^2 = 3$ GeV^2

$S_{GLS}^{pred} = 2.74 \pm 0.06$.

Because of the $1/x$ weighting, the experimental value of the integral is dominated by low-x events. We illustrate the extraction of the experimental value from data following the technique of the CCFR collaboration (49). The data are binned in fine x bins (good low-x resolution is imperative for this) and within each bin interpolated to $Q^2 = 3$ GeV^2. Figure 5 shows the values of xF_3 (right scale and squares) and the distribution of the weighted integral (left scale and diamonds) as a function of x. A fit of the form,

$$xF_3(x, Q^2 = 3) = ax^b(1-x)^c,$$

is used to calculate the unsampled, very low-x contribution to the integral. The best such fit is shown superimposed on the data in the figure. Fits are made to various functional forms (always constrained to vanish as $x \to 0$), and the integration limits are varied to estimate the systematic biases of the procedure. The overall systematic error, determined by applying the

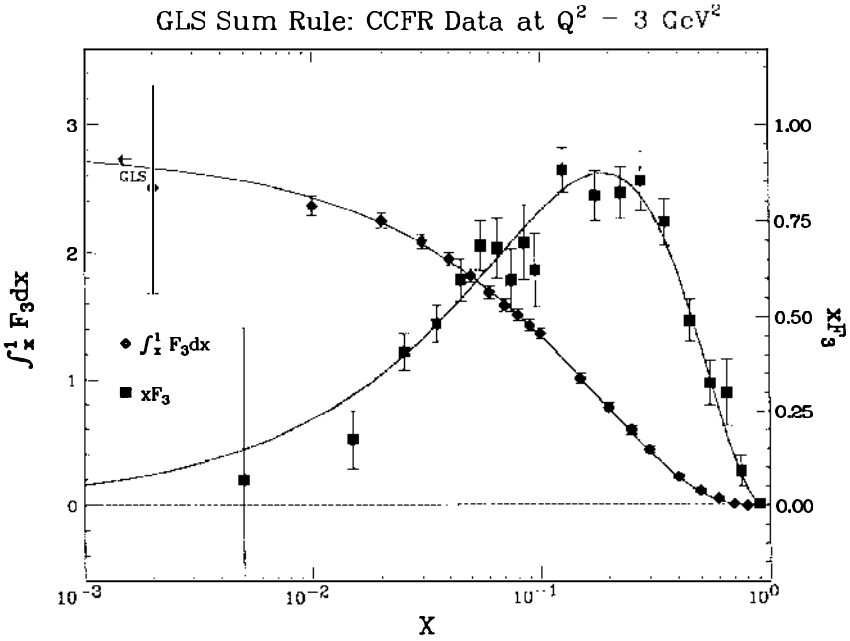

Figure 5 The xF_3 function and the GLS sum rule: The CCFR (45) measurements of xF_3 (solid squares and right scale) and the corresponding integral (diamonds and left scale) as a function of x. The dotted curve and the solid curve represent the best fit to the data as outlined in the text.

same procedure in a high statistics Monte Carlo calculation, is about a third of the statistical error.

Table 2 summarizes the published measurements (45, 49–51) of this integral. The average, excluding the CCFRR (1984) value [which is superseded by that of CCFR (1988)] is

$$\langle S_{GLS}^{expt} \rangle = 2.79 \pm 0.13,$$

which gives a difference between experiment and theory of 0.05 ± 0.14. We conclude that the GLS sum rule is consistent with the expectations of the quark-parton model and QCD at the level of the 5% experimental error.

ADLER SUM RULE The Adler sum rule, shown in Equation 8, predicts the integrated difference between neutrino-neutron and neutrino-proton structure functions. Unlike the previous case, this sum rule is expected to be valid to all orders of perturbative QCD.

The neutrino scattering measurements performed on deuterium by the WA25 (BEBC) collaboration (51) are consistent with the quark-parton model prediction,

$$S_A^{pred} = 1.$$

The experimental measurement is

$$S_A^{expt} = 0.01 \pm 0.20,$$

where we have averaged the quoted statistical and systematic errors.

GOTTFRIED SUM RULE The Gottfried sum rule, shown in Equation 9, predicts that the integrated difference between electromagnetic structure functions for neutrons and protons should be

$$S_G^{pred} = 0.33,$$

independent of Q^2. The EMC muon measurements on deuterium have

Table 2 Measurements of the Gross–Llewellyn Smith sum rule

Group (Ref.)	S_{GLS}
CDHS (1979) (50a)	3.2 ± 0.5
CHARM (1983) (50b)	2.56 ± 0.42
CCFRR (1984) (49)	2.83 ± 0.20
WA25 (1985) (51)	2.70 ± 0.40
CCFR (1988) (45)	2.79 ± 0.16

been used to test this (52a, 52b). The data, while not very precise, are in agreement with the prediction:

$$S_G^{expt} = 0.24 \pm 0.11.$$

BJORKEN SUM RULE AND SPIN STRUCTURE FUNCTION Measurements of the spin structure functions are important: they provide unique information about nucleon structure that could lead to understanding the nucleon spin in terms of the quark and gluon constituents. The Bjorken sum rule shown in Equation 10 predicts the value of the integral over the difference between appropriately weighted neutron and proton spin structure functions

$$S_B = \frac{1}{6}\frac{G_A}{G_V}\left(1 - \frac{\alpha_s}{\pi}\right) \qquad 17.$$

to have the values $S_B^{pred} = (0.191 \pm 0.002)$ for $G_A/G_V = (1.254 \pm 0.006)$ and $\alpha_s = (0.27 \pm 0.02)$, as quoted by the EMC group (53). Unfortunately, there are no measurements at present that permit a direct check of this sum rule.

The EMC collaboration has, however, reported (53) a measurement of the scattering asymmetry for a longitudinally polarized muon beam from a polarized proton target. These measurements are consistent with, but more precise than, earlier measurements (54); they extend the data into the small-x region, which is critical for the evaluation of the sum rule integral.

The asymmetry data permit evaluation of the spin structure function, $xg_1^p(x)$, characterizing the proton. Information is lacking on xg_1^n, the corresponding structure function for the neutron, which would permit a direct test of the sum rule. Even so, the measurement has generated considerable interest.

Figure 6 shows xg_1^p (right scale and squares) and the corresponding integrated value of $\int g_1^p(x)\,dx$ (left scale and diamonds) as a function of x. While there is some uncertainty in extrapolating the integral to very low x, this is not a problem unless there is some anomalous discontinuity for $x < 0.01$. With this caveat, the measured data cover about 98% of the integral. The value of the integral, evaluated at $\langle Q^2 \rangle = 10.7$ GeV^2, is

$$\int g_1^p(x)\,dx = 0.114 \pm 0.012 \pm 0.026, \qquad 18.$$

where the first error is statistical and the second is systematic.

One reason for the surprise engendered (55) by this result is that there is a sum rule by Ellis & Jaffe (56) predicting that the integral (Equation 18) should equal 0.19, as estimated by the EMC group [although estimates (55) as low as 0.17 have been quoted]. This sum rule, however, assumes

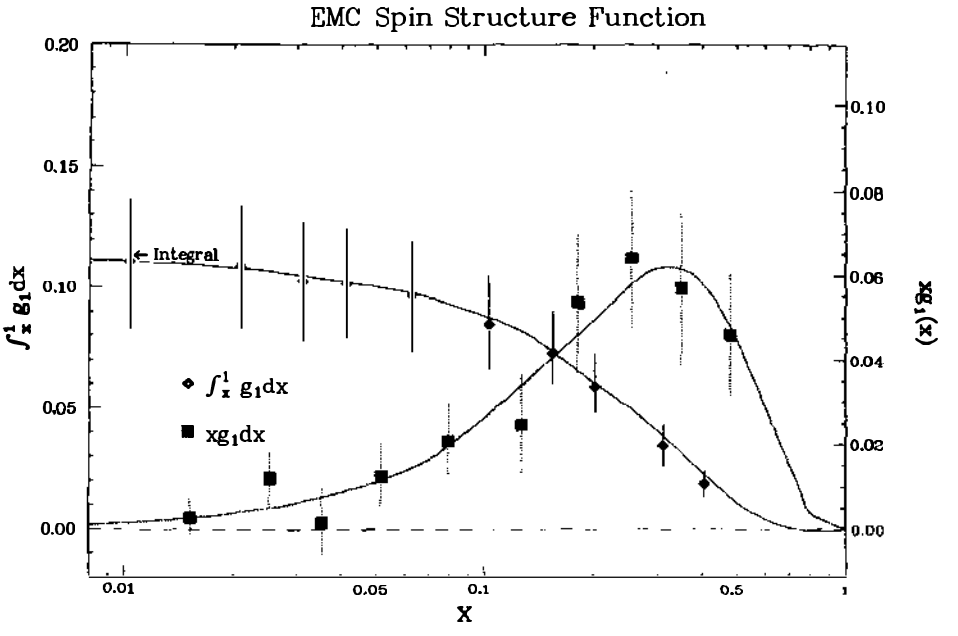

Figure 6 The EMC (53) spin structure function, $xg_1^p(x)$ (solid squares and right scale), and the corresponding integral, $\int g_1^p \, dx$ (diamonds and left scale) as a function of x.

flavor SU(3) and ignores contributions of strange quarks to the net polarization; the Bjorken sum rule, in contrast, depends only on isospin symmetry.

Assuming the validity of the Bjorken sum rule, the EMC collaboration calculates a negative value for the integrated neutron spin structure function:

$$\int g_1^n(x)\,dx = -0.077 \pm 0.012 \pm 0.026. \qquad 19.$$

Summing these two integrals and ignoring the effect of strange quarks, one infers that the net fractional spin carried on average by the valence quarks in the proton is only $14 \pm 9 \pm 21\%$. If we assume the violation of the Ellis-Jaffe sum rule is due to polarized strange quarks, the net fractional spin carried by quarks is estimated to be $1 \pm 12 \pm 24\%$. Note that for both cases the quarks carry a rather small fraction of the proton spin. This result is intuitively surprising because the nonrelativistic model of

constituent quarks has been so successful in describing the masses and magnetic moments of baryons.

There exists some controversy as to whether the violation of the Ellis-Jaffe sum rule and the apparently small fraction of the proton spin carried by quarks represent serious problems. Several authors point out that there are potentially large common contributions to the proton and neutron integrals from gluon spins (57), expected from estimates of higher order terms in the perturbative expansion. An alternative (nonperturbative) explanation, based on chiral symmetry and the $1/N$ expansion as expressed in the Skyrme model, suggests that the average quark spin and gluon spin contributions should be separately small; that is, the proton spin is principally a consequence of orbital angular momentum (58).

We note that new data with polarized leptons and polarized target nucleons would be important in clarifying these questions. Such data could be used in checking the Bjorken sum rule directly, as well as helping to understand the relationship of gluons and up, down, and strange quarks to the spin structure of the nucleon. Information from many sources may well be brought to bear on this question, including measurements of the form factors describing elastic eN scattering and pseudoelastic νN scattering (59).

3.3 *Quark Densities*

Measurements of nucleon quark densities are important for the several reasons discussed in Section 1.3. Deep inelastic scattering from heavy isoscalar nuclei provides only combinations of proton quark densities, so that measurements from light targets are required. Neutrino and antineutrino data with hydrogen (alone) provide the input for a direct method of extraction of the individual quark densities. The cross sections involve the following densities and y dependences:

$$\nu\text{p:} \quad x[d(x)+s(x)]+x[\bar{u}(x)+\bar{c}(x)](1-y)^2 \qquad 20a.$$

$$\bar{\nu}\text{p:} \quad x[u(x)+c(x)](1-y)^2+x[\bar{d}(x)+\bar{s}(x)], \qquad 20b.$$

where, for simplicity, we have suppressed the Q^2 dependence of the proton quark densities. The charm component is expected to be small in the present Q^2 domain, and hence is ignored. The strange component is accessible from the subset of events with leptonic charm decays, as discussed below. Equations 20 indicate, then, that observation of the y dependence of the cross section from neutrino and antineutrino scattering in principle permits extraction of individual u, d, $\bar{u}$, and $\bar{d}$ components of the proton.

Unfortunately, the available neutrino data are statistically limited. Electron and muon experiments have much larger event samples, but data

from both hydrogen and deuterium are necessary, and additional assumptions must be made to extract flavor-separated quark densities. For muon scattering on hydrogen, the dependence is

$$\mu p: \quad x[(d+\bar{d}+s+\bar{s})+4(u+\bar{u}+c+\bar{c})][1+(1-y)^2]/9. \qquad 21a.$$

Assuming isospin symmetry for the nucleon doublet (e.g. $u_n = d_p \equiv d$), one obtains a dependence in scattering from neutrons of

$$\mu n: \quad x[(u+\bar{u}+c+\bar{c})+4(d+\bar{d}+s+\bar{s})][1+(1-y)^2]/9. \qquad 21b.$$

Since antiquark components enter with the same y dependence as quark components, information on the antiquark part must be assumed from neutrino measurements.

Two experiments, CDHS and WA21 (BEBC), have studied $\nu/\bar{\nu}$ scattering (60a,b; see also 47) from hydrogen. Figure 7 shows the ratio of quark and antiquark components as measured by the two groups. The measurements agree at the statistical level of the experiments, which is about 15%. [For these and other comparisons, early CDHS measurements have been

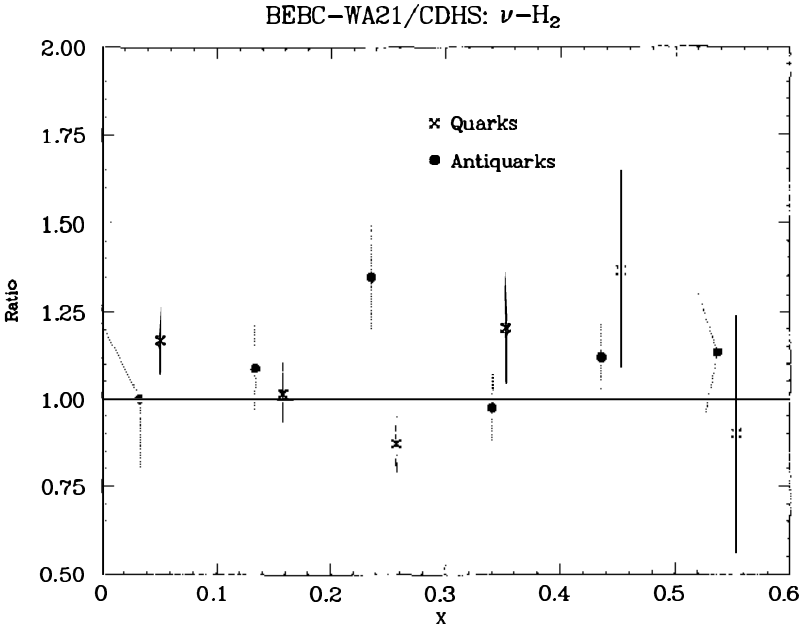

Figure 7 Ratios of the BEBC-WA21 (60b) and CDHS (60a) measurements of quark (*crosses*) and antiquark (*solid circles*) densities from ν-H_2 interactions.

adjusted in normalization to agree with their more recent measurements of the total νN cross section (61).]

There are three high statistics structure function measurements using electrons and muons on hydrogen targets (33b, 62a,b). The two muon experiments, EMC (62b) and BCDMS (33b), employing incident beam energies up to 280 GeV, reach the highest Q^2. These two measurements, however, disagree outside the statistical errors. Figure 8 shows the structure function, F_2, as a function of Q^2 in four representative x bins; $x = 0.125$, 0.250, 0.350, and 0.650 for the EMC and BCDMS data. We note that there is a discrepancy in normalization: the EMC data are lower than those of BCDMS by about 8–9% over most of the range. In addition, the two data sets exhibit a pronounced x-dependent difference. The solid curves in these figures come from an illustrative parametrization obtained from a best fit to all existing data on individual quark densities (63; W.-K. Tung, private communication).

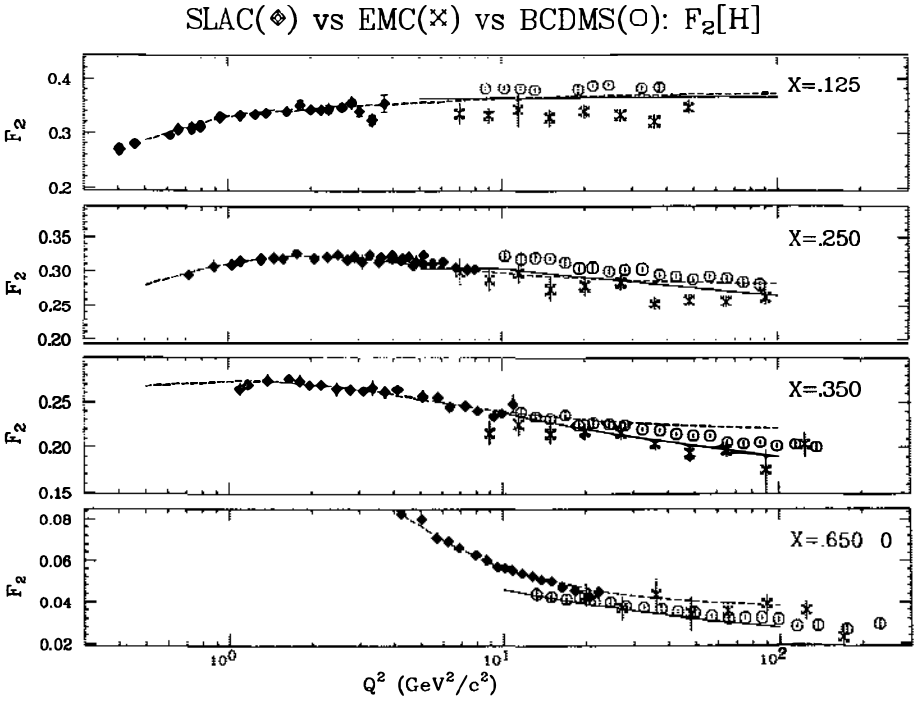

Figure 8 A comparison of SLAC (*diamonds*) (62a), BCDMS (*open circles*) (33b), and EMC (*crosses*) (62b) measurements of F_2 as a function of Q^2 in four x bins. The dotted curve shows a parametrization of the SLAC data extrapolated to high Q^2; the solid curve is an illustrative parametrization by Tung (63).

While comparing the BCDMS and EMC data to the SLAC data (shown as solid points), which admittedly are at a lower Q^2, it was noted (64) that the extrapolated fits to SLAC data, shown as dotted curves in the figure, do not fit either muon data set well. The SLAC fits are typically 9% higher than the EMC data, but generally agree with the EMC x dependence. The converse is true when the fits are compared to the BCDMS data: while the average levels agree, there is a discrepancy in the x dependence (64). Similar disagreements between the EMC and the BCDMS data are found for comparisons of F_2 measured on nuclear targets (iron and carbon respectively), as discussed at the end of this section. This glaring discrepancy between two deep inelastic muon experiments is an outstanding experimental problem and needs to be reconciled.

There are also deuterium data from SLAC (62a) and EMC (52b) evincing similar concerns: the relative x dependence of the two measurements is similar, but the EMC data consistently lie lower than extrapolated fits to SLAC data. Neutrino-deuterium data from WA25 (51) agree with EMC data (52b) within the precision of the neutrino data, except near $x \approx 0.2$.

VALENCE QUARK DENSITIES Figure 9 summarizes the available information on the separate valence quark components of the proton. Three of the four measurements are extracted from hydrogen-deuterium data with neutrinos; the fourth measurement is from the EMC muon experiment. The smooth curve is the parametrization of Tung et al (63; W.-K. Tung, private communication). The EMC valence u-quark measurements, though slightly higher than those of CDHS and WA25, agree within the statistical precision of the experiments. The valence d-quark measurements from neutrinos agree with each other; the EMC measurement, however, disagrees with those from the neutrino experiments by nearly a factor of two at $x \approx 0.2$. This discrepancy represents a problem.

The overall valence quark density for isoscalar nucleons (i.e. neutron-proton average) is essentially the xF_3 structure function measured in the high statistics neutrino experiments on isoscalar targets. The various measurements are in good agreement. This structure function was discussed in Section 3.2 and an example of one measurement is shown in Figure 5.

SEA-QUARK DENSITIES Figure 10 shows the density of one of the proton antiquark components, as obtained from the $\bar{\nu}_\mu$ hydrogen data of CDHS (60a) and WA21 (60b) and from the deuterium data (51) of WA25. The smooth curve is the Tung parametrization (63; W.-K. Tung, private communication). The statistical precision of these measurements is not very high.

The overall nucleon antiquark density $[x(\bar{u}+\bar{d})/2]$ obtained from CHDSW (46) and CCFR (45) data, shown on a log scale in Figure 11, is measured relatively precisely. There is reasonable agreement between the

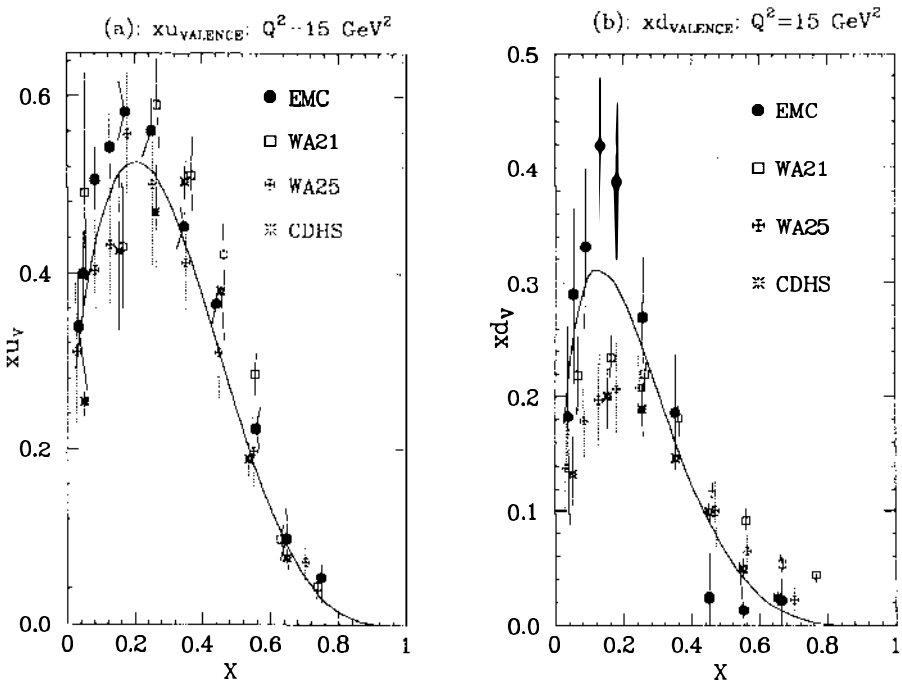

Figure 9 Valence quark densities in a proton: (*a*) xu_V; (*b*) xd_V as a function of x. The data are from EMC (52b), WA21 (60b), WA25 (51), and CDHS (60a). The solid curve is the Tung et al (63) parametrization.

CDHSW and CCFR data over most of the x range. (The lowest x values disagree because the trends of the two data sets in Q^2 are somewhat different, so that the extrapolation to $Q^2 = 5$ GeV^2 results in the differing values shown.) These antiquark distributions can be important in determinations of the gluon distribution.

MEASUREMENT OF THE STRANGE SEA Neutrino production of opposite-sign dimuons ($\mu^-\mu^+$) offers a unique probe to measure the strange component of the nucleon sea. Dimuon events originate from the production of a single charmed particle:

$$\nu_\mu + (d, s) \rightarrow \mu^- + c + X \qquad 22a.$$

$$\bar{\nu}_\mu + (\bar{d}, \bar{s}) \rightarrow \mu^+ + \bar{c} + X. \qquad 22b.$$

Here the charmed quark emerges as a charmed particle (typically D^0 and D^+), which subsequently decays, for example $D^0 \rightarrow \mu^+ + \nu_\mu + X$. The $d(\bar{d}) \rightarrow c(\bar{c})$ conversions in Reactions 22 are Cabibbo suppressed. Hence,

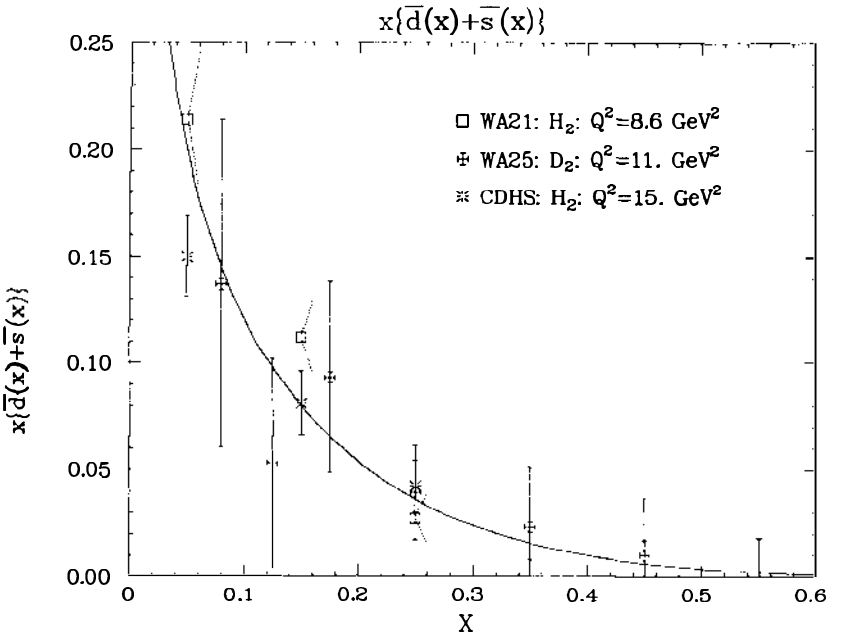

Figure 10 The antiquark component of the proton as probed by antineutrinos: $x(\bar{d}+\bar{s})$. The three sets of antineutrino data are by WA21 (60b), WA25 (51), and CDHS (60a). The curve is the Tung et al (63) parametrization.

the $\bar{\nu}$-induced $\mu^+\mu^-$ events arise predominantly from production from strange quarks ($\sim$90%), and so provide a direct measurement of the strange sea-quark density. For the ν_μ-induced events, production from s quarks competes favorably with production from valence d quarks. The ratio of the $\mu^+\mu^-$ events relative to single-muon events provides a measure of the momentum fraction, κ, carried by the strange sea quarks relative to that carried by the nonstrange sea:

$$\kappa = 2s/(\bar{u}+\bar{d}). \qquad 23.$$

If there were no strange quarks, $\kappa = 0$; if the sea were flavor-SU(3) symmetric, $\kappa = 1$. Certain model assumptions are required to extract κ from the dimuon data: (*a*) a model of the threshold dependence for charm production; and (*b*) the function describing the charm fragmentation into D mesons. In addition, the product of the parameters $B|V_{cd}|^2$ enters. Here, B is the semileptonic D-decay branching ratio for the appropriate admixture of D^+ and D^0, and V_{cd} is the Kobayashi-Maskawa matrix element connecting the charm and down quarks. The usual choice for (*a*)

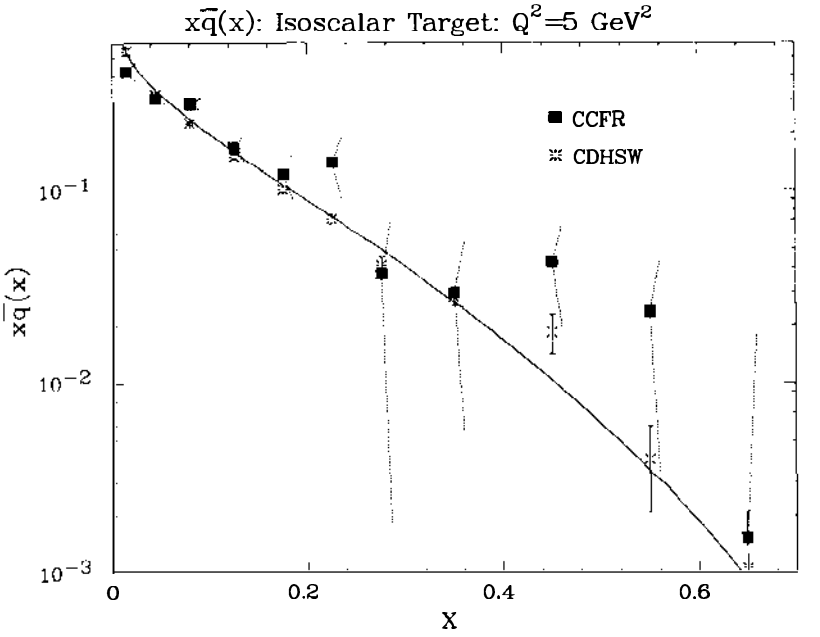

Figure 11 The antiquark density of an isoscalar target. The data shown are from the CDHSW (46) and CCFR (45) collaborations. The curves are from the Tung et al (63) parametrization.

is the "slow-rescaling" formulation, which has a single parameter, m_c, an effective charm-quark mass for this process (65–67).

The parameter, κ, is extracted from the x distributions of the dimuon events. (Some resolution effects must be unfolded since the neutrino from the charm decay is unobserved.) Figure 12*a* (12*b*) shows recent, high statistics CCFR (68) x distributions of ν_μ- ($\bar{\nu}_\mu$)-induced $\mu^+\mu^-$ events after correcting for resolutions and backgrounds. The individual contributions from valence and sea components from the fits are shown as smooth curves. The recent results on κ and $B|V_{cd}|^2$ from the CCFR collaboration's wide band data, along with their earlier CCFRR narrow band results (69) and those of the CDHS group (70), are presented in Table 3. The quoted errors include contributions from statistical and systematic sources.

These measurements of κ are in good agreement; they demonstrate that the nucleon sea has half as many strange quarks as nonstrange quarks [or is roughly one half SU(3) symmetric]. The average value for the strange sea fraction from CDHS and CCFR is

$$\kappa = 0.52 \pm 0.07. \qquad 24.$$

The value of B can also be independently calculated (69) using emulsion

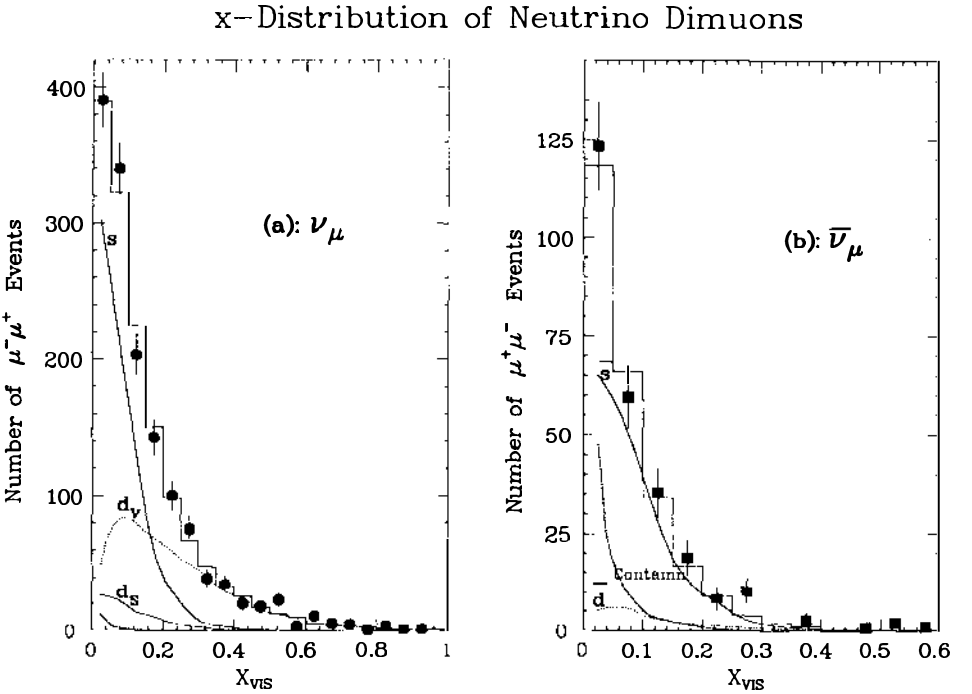

Figure 12 CCFR (65–67) x_{VIS} distribution of $\mu^-\mu^+$ events: (*a*) ν_μ-induced dimuon data (*solid circles*) after background subtraction (from π/K decays); the histogram is the charm Monte Carlo prediction, which is a sum of contributions from strange quarks (*upper solid curve*), valence d quarks (*upper dotted curve*), sea d quarks (*lower solid curve*), and contamination from antineutrino-induced events (*lower dotted curve*). (*b*) $\bar{\nu}_\mu$-induced dimuon data (*solid squares*) and corresponding Monte Carlo (*histograms*). The contributions to the Monte Carlo are from the antistrange quarks (*solid curve*), $\bar{d}$ (*lower dotted curve*), and contamination (*upper dotted curve*).

data (71) on neutrino production of charmed particles and the muonic branching fractions (72) for charmed hadrons, giving $B_{calc} = 0.110 \pm 0.009$. Evaluation (73) of $|V_{cd}|$ follows by using B_{calc}. This technique is currently the only direct measure of this parameter. The last column in Table 3 shows the resulting values of $|V_{cd}|$. The average is

$$|V_{cd}| = 0.21 \pm 0.014. \qquad 25.$$

In the limiting case that two of the three angles in the Kobayashi-Maskawa matrix approach zero, this value would approach sin θ_c, where θ_c is the Cabbibo angle.

Table 3 Values of κ and B from neutrino-induced $\mu^+\mu^-$ events

Group (Ref.)	κ	$B\|V_{cd}\|^2$	$\|V_{cd}\|$
CDHS (70)	0.52 ± 0.09	$(0.41 \pm 0.07) \times 10^{-2}$	0.19 ± 0.02
CCFRR (69)	$0.52^{+0.17}_{-0.15}$	assumed	
CCFR (68)	$0.53^{+0.13}_{-0.09}$	$(0.51 \pm 0.09) \times 10^{-2}$	0.22 ± 0.02

in a free nucleon are different from those measured in a heavy nuclear target. This was first demonstrated by the EMC collaboration (74) and corroborated by the Rochester-SLAC-MIT group (75). The "EMC effect," which states that the structure function is dependent at the 10% level on the details of the nuclear atomic number, A, is now established. It has engendered many theoretical conjectures [for a review of nuclear effects in deep inelastic scattering, see for example (76)]. Among these conjectures are (*a*) "Q^2 rescaling," which asserts that the effective momentum transfer in heavy nuclei is different from that in a free nucleon; and (*b*) that virtual pions and other hadrons within the nucleus give a larger antiquark component than for free nucleons.

The salient features of the EMC effect are illustrated by various data sets in Figure 13 (75, 77a,b). The tendency of the ratio of structure functions for a nucleus of atomic weight A to that for the deuteron, $F_2(A)/F_2(D)$, to decrease for $x < 0.15$ is presumably caused by nuclear shadowing (78), a well-known effect that is responsible for the A dependence of photon ($Q^2 = 0$) cross sections. In the intermediate x range ($0.15 < x < 0.60$), there is a clearly decreasing ratio that can be understood by a variety of mechanisms such as those mentioned above. For $x > 0.60$, the ratio increases as a result of Fermi motion.

The agreement in the crucial intermediate x region among these various experiments performed at widely different energies is nontrivial. The SLAC data cover the range $2 \leq Q^2 \leq 15$ GeV^2, while the muon scattering data cover $14 \leq Q^2 \leq 200$ GeV^2, a factor of about ten higher. It seems likely, therefore, that this effect is largely independent of Q^2. A recent measurement of $R = \sigma_L/\sigma_T$ for various nuclear targets demonstrated that this quantity does not differ for light and heavy nuclei (79).

Neutrino interactions can distinguish quark flavors and hence would be ideally suited to study the EMC effect. Neutrino measurements (80) of $F_2(A)/F_2(D)$ are consistent with those made with charged leptons. The statistical precision of these experiments, however, falls short of shedding light on nuclear shadowing (low-x behavior), or of precisely measuring antiquark composition at larger x values where the competing mechanisms (*a*) and (*b*) may differ.

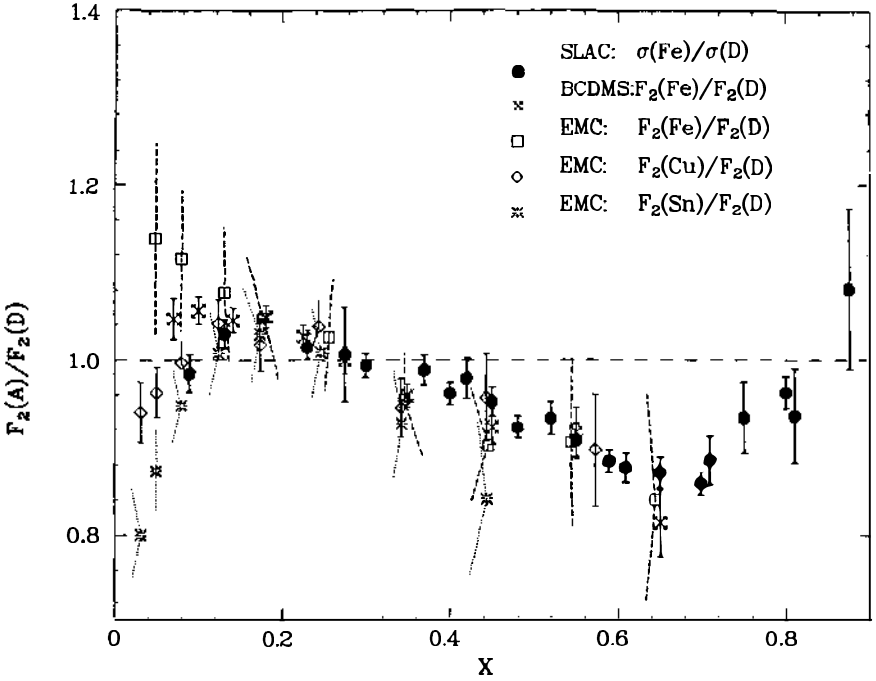

Figure 13 The EMC effect illustrating dependence of $F_2(A)/F_2(D)$ as a function of x. The data shown are those of SLAC (75), BCDMS (77b), and EMC (77a).

4. QCD TESTS AND MEASUREMENTS

4.1 *Measurements of* $R = \sigma_l/\sigma_t$

It is expected from the arguments of Section 1.5 that the value of R should be small ($R \ll 1$). Furthermore, for x fixed and low Q^2, R should fall as a power of $1/Q^2$; at higher Q^2, R should fall as the logarithm of Q^2. The earliest low-Q^2 measurement from SLAC (3) did obtain a small value ($R \approx 0.18$) as anticipated from the Callan-Gross prediction; this was the first direct demonstration of spin-1/2 constituents for hadrons. On the other hand, subsequent measurements (81; earlier articles include 3, 62a, 82) of R at SLAC seemed nearly independent of Q^2, although the systematic uncertainties were large. Measurements with neutrino and muon beams at higher Q^2, as discussed below, gave smaller values of R. The situation has been perplexing for two reasons: (*a*) the continuity of all these measurements was questionable; and (*b*) a flat Q^2 dependence is difficult to reconcile with any reasonable model of spin-1/2 constituents.

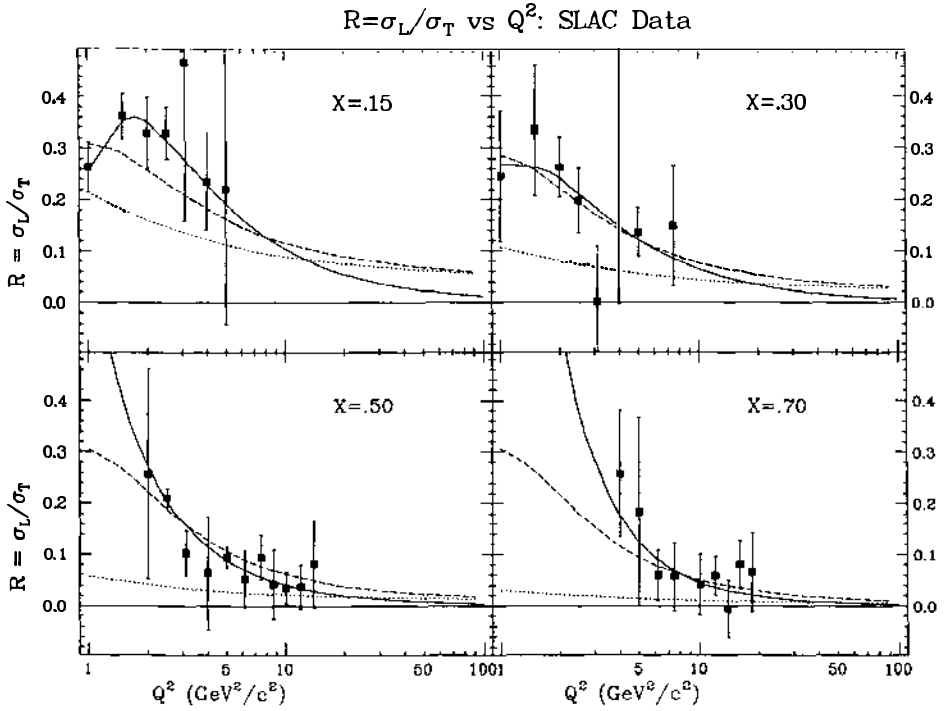

Figure 14 The SLAC (83) data showing $R = \sigma_l/\sigma_t$ as a function of Q^2 in four representative x bins. The lowest dotted curves represent predictions from the QCD calculation (see footnote 5), the dashed curves represent QCD prediction with a higher twist contribution; the solid curves represent a higher twist fit of the type shown in Equation 26 without the perturbative QCD term.

Recent measurements taken at SLAC have provided a new perspective to this historical problem. The new data (83), shown for a subset of x values in Figure 14, qualitatively show the expected behavior at low Q^2. The lower dotted curves are the predictions of a QCD calculation (see Equation 13) used by the experimenters. As expected, nonperturbative effects contribute heavily to the experimental data in this low-Q^2 regime. The upper dashed curve includes a higher twist term fitted to the data.[5] The authors

[5] The QCD prediction and the empirical fitted term used by Dasu et al (83) is

$$R(x, Q^2) = \frac{1.11(1-x)^{3.34}}{\ln(Q^2/0.04)} + \frac{0.11(1-x)^{-1.94}}{Q^2},$$

where the first term is an approximate parametrization of Equation 13 and the second term comes from an empirical fit to the SLAC data.

indicate, and the figure illustrates, that this hypothesis fits the data well. On the other hand, these data do not demonstrate the predicted perturbative QCD behavior (lower dotted curves). The measured values of R at these low Q^2 are evidently due principally to higher twist effects.

We have used this SLAC data to predict the value of R with the hypothesis that all the Q^2 dependence in the SLAC data is described by higher twist (85). This is useful in judging whether other existing data at higher Q^2 require a QCD explanation. We adopt the parametrization for the higher twist

$$R_{HT} = \frac{\alpha(x)}{Q^2} + \frac{\beta(x)}{Q^4}. \qquad 26.$$

The resulting fitted values of α and β at each x value were then used to calculate the solid curves shown in Figure 14. These fits are quite acceptable; furthermore, the values of α and β are typically in a reasonable range for the higher twist hypothesis; i.e. $\alpha < 1$ GeV^2 and $\beta < 1$ GeV^4. The fitted values of $\alpha(x)$ and $\beta(x)$ provide an estimate of the maximum effect that higher twist could have at the higher Q^2 of other experiments. Typically, this hypothesis predicts a small value of R_{HT} when $Q^2 > 10$ GeV^2, as expected.

Averaged values of the high-Q^2 data on R are shown as a function of x in Figure 15 (32c, 33b, 86–88). The data point at a given x usually consists of averaged points from many different values of Q^2. The data cover the range $0.015 < x < 0.65$ and $1.4 < Q^2 < 70$ GeV^2. Not surprisingly, the data with the largest positive excursions from zero are at the lowest Q^2. Overall, detailed comparison of the data contained in Figure 15 with R_{HT} gives an acceptable χ^2. For a fit to the QCD hypothesis with inclusion of the higher twist effects described previously,[5] and χ^2 is no better.

We conclude that the qualitative behavior of data on R agrees well with quark model expectations that R should be small and falling with Q^2. The behavior at higher Q^2 should follow the quantitative expectations of QCD, but the data are not yet precise enough to verify this prediction.

4.2 *Scaling Violations in Nonsinglet Structure Functions*

In the Q^2 domain where perturbative QCD is expected to apply, Equation 14 states that, for nonsinglet structure functions, the logarithmic derivative with respect to Q^2, at fixed x, should be a predictable function:

$$\frac{d \ln xF_3(x, Q^2)}{d \ln (Q^2)} = \psi(x, Q^2). \qquad 27.$$

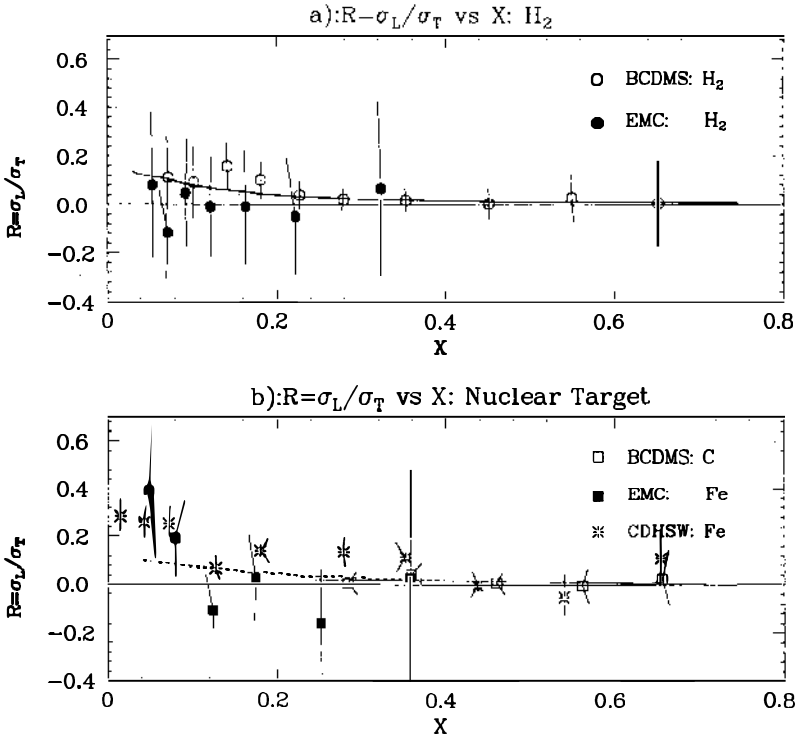

Figure 15 Measurements (33b, 86–88) of R at high Q^2: (*a*) hydrogen, (*b*) nuclear targets as a function of x. Data at many differing Q^2 values have been averaged at each value of x.

The term $\psi(x, Q^2)$, shown up to leading order in Equation 14, involves an integral of the $\xi F_3(\xi, Q^2)$ structure function for all values $\xi > x$. This integral is calculated, either directly or using a fit, from the same data used for the logarithmic derivative on the left-hand side. In principle, the only unknown in $\psi(x, Q^2)$ is α_s, which in turn is known as a function of Λ (Equation 12). Figure 16 illustrates this for a particular parametrization of xF_3. Note that a specific curve exists for a specific value of Λ.

Figure 16 also shows the slopes extracted from the CDHSW wide band data (46) for xF_3 as a function of x for $Q^2 > 6$ GeV^2. These data, which come from the largest statistical sample published, are superimposed on the same family of curves. Note that no curve agrees well with the data. The figure also shows the narrow band data of CCFR (45). Here, disagreement is not obvious, but the statistical precision is not as high as the wide band CDHSW data. New wide band data at very high Q^2 from CCFR should help in addressing this question.

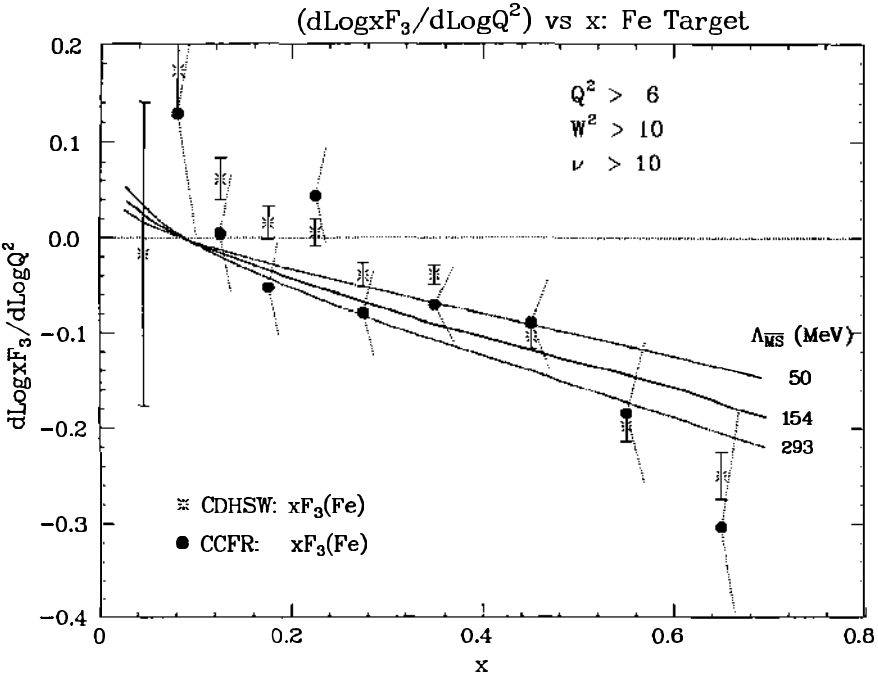

Figure 16 The measured logarithmic derivative of xF_3 with respect to Q^2 as a function of x, reported by the CDHSW (46a) and the CCFR (45) collaborations. QCD predictions, for specific values of $\Lambda_{\overline{MS}}$, are shown by the solid and dotted curves.

It should be noted that the curves in Figure 16 are calculated in next-to-leading order of the perturbative expansion. (The general features are the same in leading order.) However, no corrections for higher twist have been applied because such effects are not well understood. Such higher twist corrections, if they exist, must fall with a power of $1/Q^2$. Their contribution would be much reduced if the data were restricted to higher momentum transfers. When such a cut, say $Q^2 > 20$ GeV^2, is applied, the statistical precision of the CDHSW data is such that, while consistent with the requirements of QCD, the test is not very stringent.

4.3 *Scaling Violations in Singlet Structure Functions*

The evolution of singlet structure functions (e.g. F_2) follows equations more convoluted than Equation 14, because of the presence on the right-hand side of an additional integral over the gluon distribution. This can be viewed as either a problem or a bonus. On the one hand, it complicates

any test of QCD behavior; on the other hand, under the assumption that QCD behavior is valid and well understood, it permits extraction of the gluon distribution. Techniques have been developed to test QCD with singlet structure functions for two reasons: (*a*) because the statistical precision is so much better in neutrino F_2 measurements relative to those of xF_3, and (*b*) because xF_3 is not available from muon scattering experiments.

The procedure followed by the BCDMS group (33a,b,c) is typical. First, note that in regions of large x, we anticipate that $R \to 0$, $\bar{q} \to 0$, and $G \to 0$. In such a limit, $F_2 \to xF_3$, and the evolution equation should look identical to that for a nonsinglet. The BCDMS group uses data for $x > 0.275$ and $Q^2 > 20$ GeV^2. The comparison of d (ln F_2)/d (ln Q^2) for the BCDMS data on hydrogen and on carbon is shown in Figure 17 with the corresponding QCD predictions. The agreement is extremely good; the

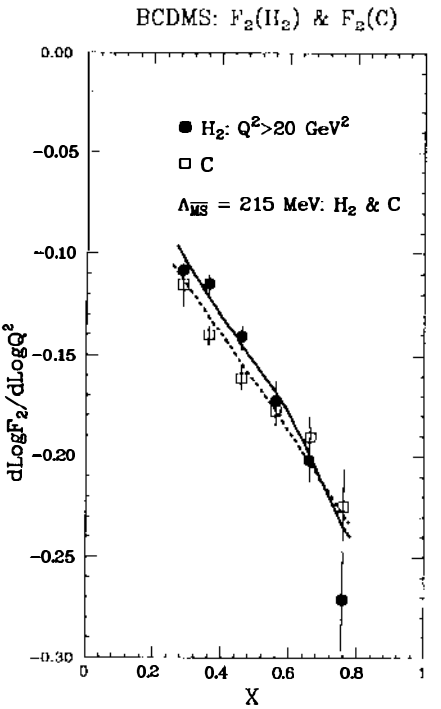

Figure 17 BCDMS (33b,c) measurement of the logarithmic derivative of F_2 with respect to Q^2 vs X with H_2 (*solid*) and C (*open*) targets. The corresponding QCD predictions are shown by solid and dotted curves, respectively.

small predicted differences (due to the differences in the F_2 shape) between hydrogen and carbon seem to be followed by the data.

This procedure, applied to the EMC data (32c) with $Q^2 > 10$ GeV^2, yields the comparison between data and prediction shown in Figure 18*a*. Note that the entire trend of the data is unlike the predicted curve. A similar comparison occurs for the F_2 structure function of CDHSW shown in Figure 18*b*. At face value, the EMC and CDHSW data question the predictive capability of perturbative QCD, at least in this Q^2 regime. We discuss the conflicts among these data below.

For hydrogen data, the BCDMS measurements extend down to low x. In Figure 19, we see the logarithmic slope data plotted into the low-x region. The lower curve is the prediction for the nonsinglet case; the difference between the lower curve and the data is attributed to the effect of gluons at low x. It should be noted that the procedure has assumed that

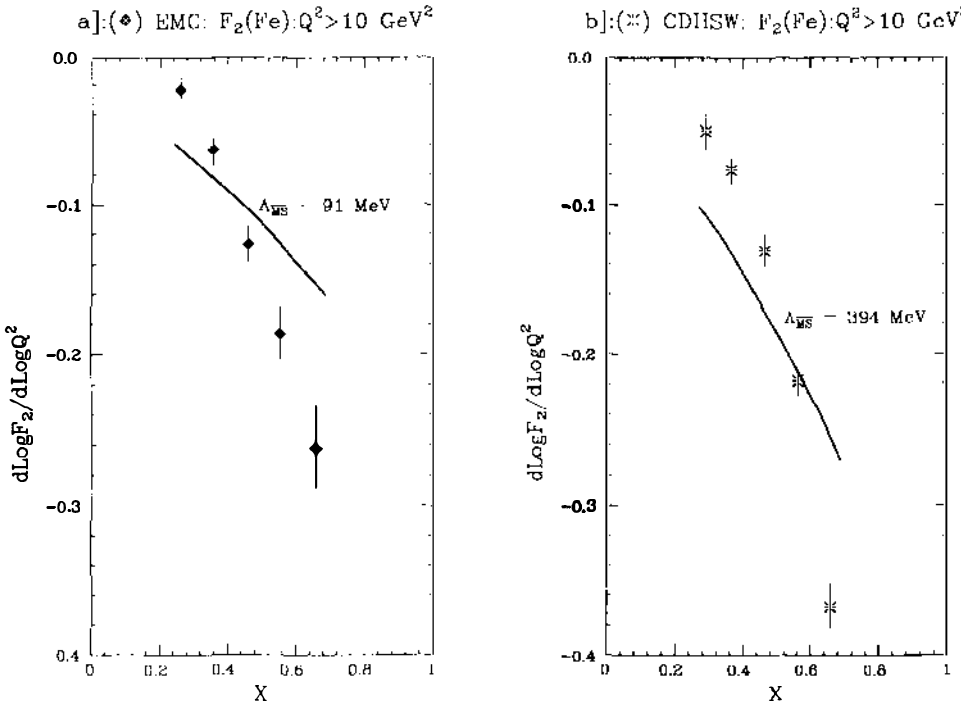

Figure 18 The logarithmic derivative of F_2 with respect to Q^2 vs x with an iron target as measured by (*a*) EMC (32b) and by (*b*) CDHSW (46a) collaborations. The QCD curves with typical values of $\Lambda_{\overline{MS}}$, as analyzed by the BCDMS collaboration (33c), are also shown.

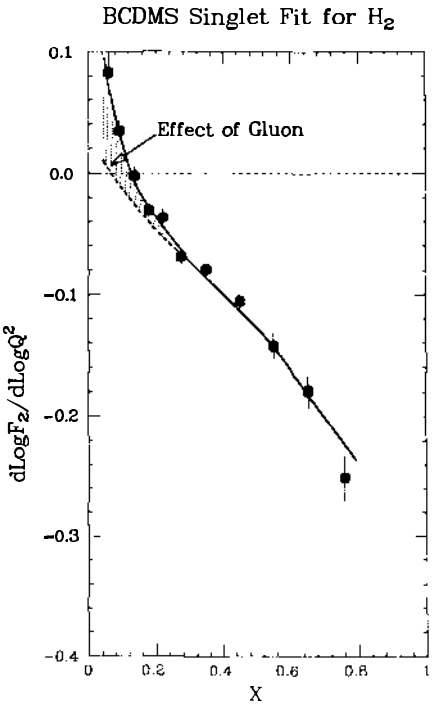

Figure 19 The BCDMS (33b,c) measurements of the logarithmic slope of F_2 for H_2 target. The perceived effect of the gluons, prominent at low x, is shown by the hatched region between the singlet (*solid*) and the nonsinglet (*dotted*) QCD predictions.

$G = 0$ for $x > 0.275$ and so the calculated gluon distribution must be very small in that region; the assumption cannot be verified from the same data.

The fits to the BCDMS data, treated as nonsinglets in the large-x region, in next-to-leading order, give the results

$$\Lambda_{\overline{MS}} = 230 \pm 20 \pm 60 \text{ MeV for carbon;}$$

$$\Lambda_{\overline{MS}} = 200 \pm 22 \pm 60 \text{ MeV for hydrogen.}$$

4.4 *Experimental Conflict on Structure Function Evolution*

The preceding discussion indicates a clear conflict between conclusions from the BCDMS muon scattering experimental results in Figure 17, on the one hand, and from EMC (μ scattering) and CDHSW (ν scattering) data in Figure 18, on the other. (The narrow band data from CCFR do

not have enough statistical precision to permit a definite conclusion; CCFR Tevatron wide band data are still being analyzed.) While the BCDMS data show a logarithmic dependence that is consistent with the predictions of QCD, the EMC and CDHSW data clearly do not. The data in Figure 18 show a slope at large x ($x > 0.55$) that is much more negative than predicted by QCD, and a slope at intermediate x ($x < 0.45$) that is nearer zero than predicted.

Attempting to ascribe a precise cause for this conflict would be mere speculation. It is interesting, however, to detail some differences among the experiments, which is done in Table 4. Note that other experiments (like CCFR, CHARM, and BFP), which are more similar to the first column than the second, do not at present lend substantial weight to either side of the controversy.

The use of carbon rather than iron should be inconsequential, as discussed below. However, the energy measurement is very important. Because of the geometry of the BCDMS experiment, the final-state hadronic energy must be inferred from the difference between the beam and outgoing muon energies. This imposes a very strong requirement on the precision of the muon energy measurements, particularly in regions where ν is small (larger x and smaller Q^2). The toroidal magnetic field used for the measurement is calibrated to a precision of 2×10^{-3}, which is not adequate. So data from differing muon energies are used to make a final adjustment. If the R parameter were known and the calibration correct, differing incident muon energies should give precisely the same structure functions at the same values of x and Q^2. An incorrect value of R would give a pattern of structure function differences distinct from the pattern of differences resulting from an incorrect calibration. In the case of the carbon data, a final adjustment of 1.0013 was made in the magnetic field value, based on these considerations (33b). The BCDMS experimenters make a convincing argument that this final calibration adjustment can be performed without bias.

Table 4 Experimental differences among experiments

Experimental feature	CDHSW and EMC	BCDMS
Target material	Iron	Carbon
Energy measurement	E_μ magnet ν calorimetry	E_μ magnet $\nu = E_\mu - E_{\mu'}$ with $E_{\mu'}$ measured to about 10^{-3}
Q^2 range	Q^2 down to 10 GeV^2 or lower	$Q^2 > 25$ GeV^2

The validity of perturbative QCD in deep inelastic scattering is not settled. There are differing conclusions from the experiments. Several resolutions of the experimental conflict have been proposed:

1. "Iron is different from Carbon." We recall that the test (Equation 14) has only to do with the validity of the evolution equation. In principle, this equation should be valid for any "bag of quarks and gluons," so long as the evaluation of the integral on the right-hand side is characteristic of the same bag as the data on the left-hand side, and the integration is being done correctly. It should not matter which bag of quarks is used, provided higher twist effects can be ignored. It is difficult to understand how a specifically nuclear effect could create higher twist terms that persist beyond $Q^2 \approx 10\ \text{GeV}^2$. Suggestions have been made (43b) that there might be a difference between carbon and iron that has a logarithmic Q^2 dependence. Such an effect must be QCD in origin and would imply that the evolution equations for carbon and iron are different. It is difficult to conceive how conventional quantum chromodynamics could accommodate this. In any case, comparison among low-Q^2 and high-Q^2 experiments, as mentioned in Section 3.3, provides no evidence that such an effect exists.

2. "Uncorrected systematic errors" in one or more experiments might produce this difference. Such difficulties, if they exist, are unlikely to be simple. There are substantial systematic differences among these experiments, like the normalization problems between the EMC experiment and the neutrino experiments or in the x dependence and normalization conflicts between the high statistics muon experiments on hydrogen described in the previous section. In addition, different QCD evolution programs and parametrizations are often used.

3. "Different ranges of Q^2 are being compared." As noted earlier, when the higher Q^2 cut of BCDMS is imposed on the EMC or CDHSW data, the statistical precision is not really adequate to make a definitive statement; that is, the conflict largely disappears. The BCDMS data, on the other hand, do not extend to lower Q^2, where a direct numerical comparison between experimental data could be made. More data at high Q^2, from both muon and neutrino experiments, are very important.

4.5 *Measurements of the QCD Parameter,* Λ

Even though there are strong disagreements among experiments about the presence or absence of QCD-like behavior, there are no strong disagreements among the various published values of $\Lambda_{\overline{\text{MS}}}$, the value of Λ in the next-to-leading order $\overline{\text{MS}}$ scheme. Table 5 shows the values for this parameter obtained from data on the true nonsinglet

Table 5 Nonsinglet fits

Group	$\Lambda_{\overline{MS}}$ (MeV)
CDHS (1983)	200 ± 100
CHARM (1983–84)	$310 \pm 140 \pm 70$
CCFR (1984)	155^{+230}_{-130}

xF_3 structure function. The corresponding values from F_2 are shown in Table 6.

An average of values (47) from true nonsinglet fits in Table 5 is

$$\Lambda_{\overline{MS}} = 186 \pm 60 \text{ MeV},$$

which is consistent with the BCDMS average of $215 \pm 15 \pm 60$ MeV. Even the EMC values are near (within their quoted systematic errors) the BCDMS values. There is a controversy as to whether perturbative QCD describes these data; however, the values of the quark-gluon coupling do not seem to be controversial. The use of data that are marginally compatible with the stated QCD hypothesis to provide a value for $\Lambda_{\overline{MS}}$ is, of course, suspect.

5. SEARCHES FOR EXOTIC PROCESSES

5.1 *Like-Sign Dimuons*

Early measurements (69, 89–92) of neutrino-induced like-sign dimuons events,

$$\nu_\mu + N \rightarrow \mu^- + \mu^- + X,$$

with $E_\nu < 300$ GeV, posed an intriguing problem for the standard model. These measurements indicated an excess of such events over the expected backgrounds at a statistical level of two to three standard deviations. (The backgrounds were expected principally from decays of π and K mesons in

Table 6 Singlet fits

Group	$\Lambda_{\overline{MS}}$ (MeV)
EMC–Fe (1986)	$115 \pm 20^{+90}_{-45}$
EMC–H_2 (1985)	110^{+60+90}_{-50-50}
EMC–D_2 (1987)	$65^{+95+155}_{-50-45}$
BCDMS–C (1987)	$230 \pm 20 \pm 60$
BCDMS–H_2 (1987)	$200 \pm 22 \pm 60$

the hadronic showers of charged-current events.) Furthermore, the rate exhibited a tendency to increase with neutrino energy.

A signal of like-sign dimuons is expected because of associated production and decay of pairs of charmed particles. However, the perturbative QCD prediction, assuming gluon bremsstrahlung as the mechanism, fell short by almost an order of magnitude (93). It was noted (94), however, that the systematic uncertainty in the theoretical prediction could be as large as 60%, in large part because of the uncertainty in the threshold behavior of the process.

Data from the recent high statistics CCFR experiment (95), conducted at the Tevatron with neutrino energies up to 600 GeV, obviate the need for any new threshold and are consistent with, but do not require, the expected charm contribution at higher energies.

Figure 20 presents a compilation (69, 89–92, 95) of the world data along with the CCFR 90% confidence limit (CL) on the rate of production of

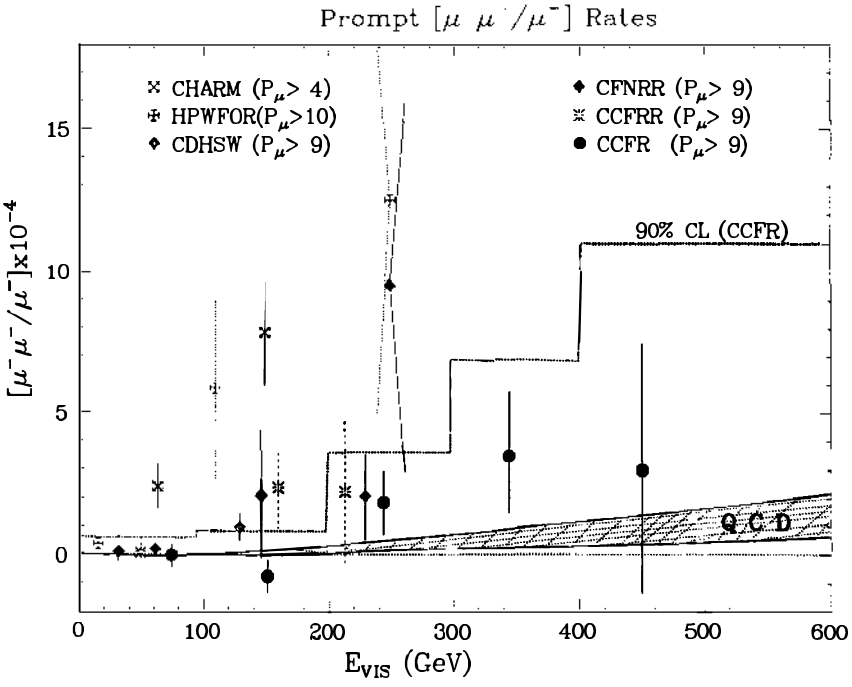

Figure 20 A compilation of the world data (69, 89–92, 95) on the rate of like-sign dimuon production with respect to single muon as a function of neutrino energy. The leading-order QCD prediction and the subsequent uncertainties are also shown (94).

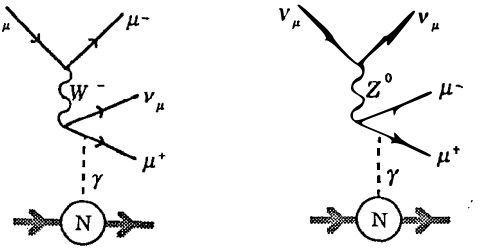

Figure 21 Feynman diagrams showing production of trileptons in neutrino scattering.

like-sign dimuons with respect to charged-current events.[6] The theoretical prediction is shown as a band signifying the uncertainty in the calculation. While like-sign dimuons no longer offer a threat to the standard model, it would be of interest to test whether the QCD prediction is correct at high energy.

5.2 *Coherent-Trilepton Production*

Neutrino-induced trilepton events are expected to be created by the coherent interaction of neutrinos in the coulomb field of the target nucleus, as illustrated in the diagrams of Figure 21. Such events would be characterized by a charged lepton pair ($\mu^-\mu^+$) and no visible hadron energy in the final state (recoilless dimuon). This old favorite of neutrino physics has been discussed in a series of theoretical papers (97, 98). An accurate measurement of the rate for this process could corroborate the destructive interference between the $W^\pm$ and the Z^0 diagrams shown in Figure 21, which is expected to create a 40% suppression relative to the rate predicted by the older V-A theory (W exchange alone). Confirmation of a related effect has been quoted in $\nu_e e^-$ scattering at the 2.7-standard-deviation level (44).

Two collaborations, CHARM and CCFR, have reported observation of recoilless dimuons (99). The CCFR data, shown in Figure 22, exhibit an excess of 13 dimuon events for $E_{had} < 2$ GeV, with an estimated background of 2.3 events from incoherent sources. The standard model prediction for coherent trileptons is 5.0 ± 1.5 events. The CHARM experiment

[6] The only data that show a serious statistical conflict with QCD are those of the CHARM group, with more than a three-standard-deviation difference from the prediction. While this might be attributed to differences in experimental cuts, like the lower muon threshold accepted in CHARM, it is unlikely that this is the source of the discrepancy. It has been pointed out (92) that the background subtraction made by the CHARM group for meson decays is substantially smaller than that made by other groups. Background sources that emanate directly from the event vertex have not yet been addressed in published results from the CHARM data.

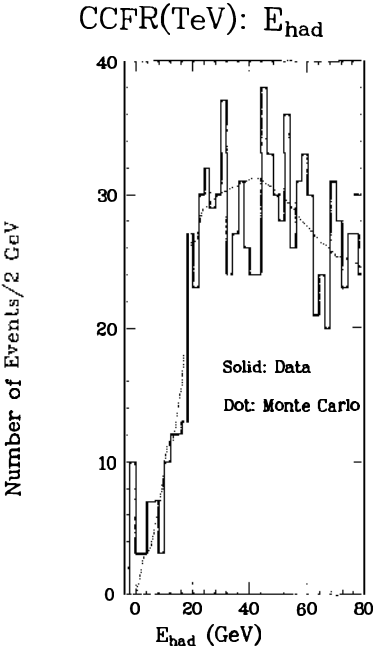

Figure 22 Distribution of hadron energy CCFR (95) of $\mu^-\mu^+$ events. The excess data (*histograms*) over conventional Monte Carlo (*dotted curve*) below 2 GeV represent the recoilless dimuons.

reports similar statistical precision. Thus the available data corroborate the existence of coherent trileptons but do not yet confirm the standard model prediction of destructive interference. Both collaborations have in hand substantially increased statistical samples to address this important question.

5.3 *Search for Neutral Heavy Leptons*

Deep inelastic neutrino scattering provides a unique mechanism for producing and detecting specific types of neutral heavy leptons (η) (100), like those motivated (101) by grand unified theories, string phenomenology, or certain left-right symmetric theories. The coupling of such leptons to the ordinary neutrino is assumed to be suppressed relative to that of the ordinary weak interactions by a factor U; this suppression could be visualized as due to the mismatch of the two different lepton "types" (e.g. differing weak-isospin charges or helicities). The effect of $U < 1$ would be to reduce the production cross section and to increase the lifetime. Searches for leptons of lower mass are best conducted in hadron decay experiments:

(*a*) $\pi \rightarrow \eta + \mu$ at SIN (102),

(*b*) $K \rightarrow \eta + X$ at KEK (103a) and LBL (103b) and

(*c*) $D \rightarrow \eta + X$ in a beam dump experiment at CERN (104a,b).

These searches are principally limited by the mass of the parent meson, so they provide the most sensitive limits for masses below about 1.8 GeV. High energy ν_μ-N experiments are most sensitive for high mass NHL searches. In this article, we concentrate upon these. The search is conducted in two channels (105):

(*A*) $\eta \rightarrow \mu^- + \mu^+ + X$,

with an assumed branching ratio (105, 106) of 10% and kinematics distinct from events due to conventional hadronic sources; and

(*B*) $\eta \rightarrow \mu^- + X$ and $\eta \rightarrow \nu + X$,

with assumed branching ratios of 55% and 21%, respectively (105, 106). The sensitivity occurs for those cases in which the lifetimes are long enough so that a decay vertex would appear far enough downstream of the production vertex to result in two clearly distinguished vertices.

Figure 23 shows 90% C.L. upper limits on neutral lepton production from several sources. The CCFR limit from (*A*) excludes masses up 18 GeV for full coupling, while the sensitivity to the coupling strength (U^2) extends below 10^{-3} for a mass of 2 GeV. The null result of the double vertex search conducted by the CHARM and CCFR collaborations are also shown in the figure.[7] New data should permit these searches to extend to masses of 22 GeV at full coupling and provide coupling limits as low as $U^2 \approx 10^{-6}$ for lower masses.

6. SUMMARY AND CONCLUSIONS

Deep inelastic scattering has been and continues to be a fertile process for seeking out new phenomena, a vital testing ground for the predictions of the standard model, and an important laboratory for measuring many of the important parameters of the prevalent theory. Beginning with the pioneering SLAC experiments and continuing with experiments of higher precision and higher energy conducted at SLAC, FNAL, and CERN,

[7]These limit curves should be closed figures in this plane. The double valued nature is due to two competing effects. For a given mass, if the coupling (U) were large, η would decay too quickly to leave a distinct second vertex; alternatively, if the coupling were too small, the lepton would escape the detector without decaying. We have shown the incomplete curves quoted by the authors.

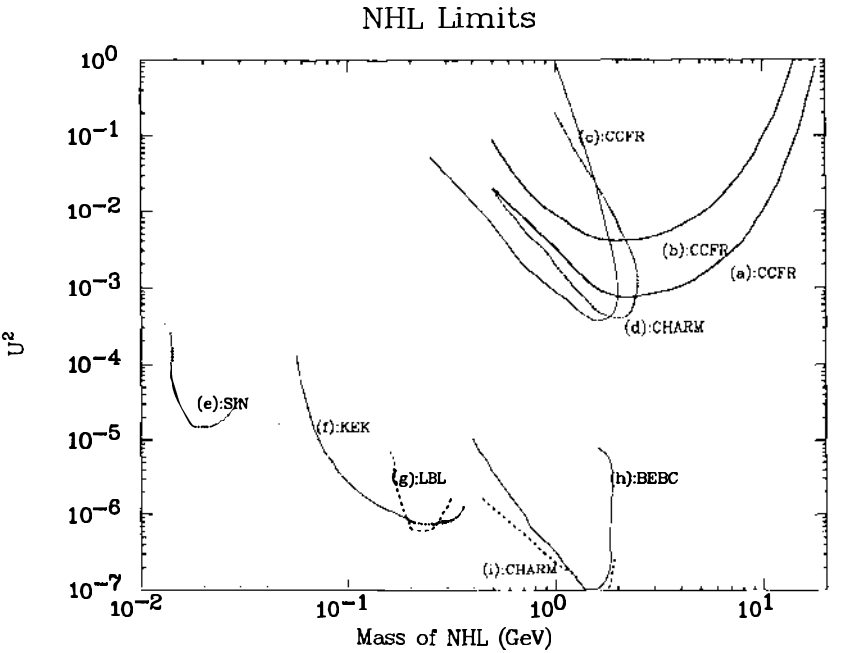

Figure 23 Upper limits (at 90% C.L.) on the neutral heavy lepton coupling, U^2, as a function of its mass by CCFR (100, 105) ν_μ-N interactions (curves *a*, *b*, *c*); CHARM (104b) neutrino interactions and beam dump (curves *d*, *i*); BEBC (104a) beam dump (curve *h*); LBL (103b) K decay (curve *g*); KEK (103a) K decay (curve *f*); and SIN (102) π decay (curve *e*).

these studies have demonstrated the validity of the electroweak theory and the quark structure of nucleons. Furthermore, experiments are in the process of testing the predictions of QCD. A short synopsis of the status of the various topics follows.

The universality of nucleon quark densities is verified by the data. The spin of the scattered quarks is 1/2 ($R \ll 1$). The mean-square charge of the quarks, derived from neutrino and muon scattering, is 5/18 at the 10% level. The number of valence quarks (GLS sum rule) is three to high precision. Two other sum rules, those of Adler and Gottfried, are consistent with measurements. The fundamental Bjorken sum rule, which quantifies the "spin states" of a nucleon invoking only the isospin symmetry, has not yet been tested, but the recent measurement of the proton spin structure function by EMC may well lead to a new understanding of the distribution of nucleon spin among the constituents. New experiments to measure the proton and neutron spin structure are eagerly awaited.

The several neutrino measurements of quark densities agree within their present statistical precision. The more abundant muon data, however, exhibit two outstanding inconsistencies: (*a*) the lack of agreement in the normalization and shape of $F_2(x, Q^2)$ between BCDMS and EMC data; and (*b*) the discrepancy between the valence d-quark measurement by the EMC on one hand, and by neutrino experiments (WA21, CDHS, and WA25) on the other. Even though there are systematic problems at the statistical level of these experiments, the agreement among them is still comparable to the statistical precision of the several neutrino experiments. These problems may be resolved with improved analysis and new data.

The nuclear dependence of nucleon structure function, the EMC effect, is now firmly established from various measurements using muons and electrons. Neutrino experiments will have to reach a new level of precision to distinguish between competing theoretical models. The structure functions at low and intermediate values of x scale not quite linearly with atomic weight. Also, measurements ranging more than a factor of 10 in Q^2 show no clear dependence on this parameter.

Measurements of $R = \sigma_L/\sigma_T$ are consistent with, but do not demonstrate, the predictions of perturbative QCD. The recent measurements at SLAC have clarified the low-Q^2 behavior of the parameter, as well as demonstrating its nuclear independence. More precise data at high Q^2 are needed to test QCD predictions unequivocally.

QCD predicts the x dependence of the slope of the structure function evolution with Q^2 $\{d[\ln F(x, Q^2)]/d[\ln Q^2]\}$. The simplest predictions, from xF_3, do not yet have enough statistical precision at high Q^2 to warrant a strong conclusion. The present experimental data on F_2 permit the following observations: (*a*) the BCDMS data from hydrogen and carbon agree with theory; (*b*) the CDHSW neutrino data, as well as the EMC and BFP muon data on F_2, exhibit slopes that are much steeper (at high x) than predicted. The reason for this discrepancy is not understood at present; more data at higher Q^2 may clarify this important question.

The world average of the QCD parameter from nonsinglet fits (xF_3) is $\Lambda_{QCD} = 180 \pm 60$ MeV, in agreement with the corresponding BCDMS value from singlet fits, $215 \pm 15 \pm 60$ MeV.

Study of like-sign dimuons at the Tevatron has obviated any need for invoking mechanisms beyond the standard model. Recoilless dimuons have been observed and are interpreted as trilepton production. The data are not adequately precise to demonstrate the standard model prediction of W-Z destructive interference. Limits on neutral heavy leptons have improved, and searches will continue with new data.

As described in the text and summarized above, some unsettled issues of consistency with theory and some apparent contradictions among the

experiments remain to be addressed. New high statistics deep inelastic data from fixed-target experiments should substantially aid this effort, as well as exploring new regions for searching out new phenomena. Finally, with the advent of HERA, an expansion by an order of magnitude in center-of-mass energy, in momentum transfer, and in the x parameter will open. We hope that future contributions of deep inelastic scattering physics to our understanding of particles and forces will match the exciting discoveries and measurements of the past.

ACKNOWLEDGMENTS

We are pleased to thank our colleagues in the CCFR collaboration for much assistance and many helpful conversations. Special help was forthcoming from A. Bodek, and E. Oltman. Communications with F. Close, J. Ellis, P. Herczeg, W. Marciano, A. Mueller, and W.-K. Tung are also gratefully acknowledged. We especially would like to thank A. Caldwell, E. Hyatt, and S. Ritz for critical reading of the draft manuscript and many helpful suggestions. The authors are supported by funds from the National Science foundation.

Literature Cited

1. Hofstadter, R., *Electron Scattering & Nuclear and Nucleon Scattering*. New York: Benjamin (1963)
2. Gell-Mann, M., *Phys. Lett.* 8: 214 (1964); Zweig, G., *CERN Reps. 8182/TH 401, 8419/TH 412* (1964) (unpublished)
3. Miller, G., et al., *Phys. Rev.* D5: 528 (1972); Bodek, A., et al., *Phys. Rev. Lett.* 30: 1087 (1973)
4. Bjorken, J. D., Paschos, E. A., *Phys. Rev.* 185: 1975 (1969)
5. Feynman, R. P., *Phys. Rev. Lett.* 23: 1415 (1969); *Photon-Hadron Interactions*. Reading, Mass: Benjamin (1972)
6. Eichten, T., et al., *Phys. Lett.* 46B: 274 (1973)
7. Bardeen, W. A., Fritzsch, H., Gell-Mann, M., in *Scale and Conformal Symmetry in Hadron Physics*, ed. R. Gatto. New York: Wiley (1973), p. 130; Gross, D. J., Wilczek, F., *Phys. Rev.* D8: 3633 (1973); Weinberg, S., *Phys. Rev. Lett.* 31: 494 (1973)
8. Weinberg, S., *Phys. Rev. Lett.* 19: 1264 (1967); Salam, A., In *Elementary Particle Theory: Relativistic Groups and Analyticity (Nobel Symp. No. 8)*, ed. N. Svartholm. Stockholm: Almqvist & Wiksell (1968), p. 367
9. Hasert, F. J., et al., *Phys. Lett.* 46B: 138 (1973)
10. Barish, B. C., et al., *Proc. 17th Int. Conf. on High Energy Physics*, London (July 1974), p. 111; Barish, B. C., et al., *Phys. Rev. Lett.* 34: 538 (1975)
11. Prescott, C. Y., et al., *Phys. Lett.* 84B: 524 (1979)
12a. Fogli, G. L., *Riv. Nuovo Cimento* 9(8): 1–67 (1986)
12b. Sirlin, A., in *Proc. Int. Symp. on Lepton-Photon Interactions at High Energy*, Hamburg (1987)
12c. Amaldi, U., et al., *Phys. Rev.* D36: 1385 (1987)
13. Perkins, D. H., *Introduction to High Energy Physics*. Reading, Mass: Addison-Wesley (1982), pp. 287–305; Fisk, H. E., Sciulli, F., *Annu. Rev. Nucl. Part. Sci.* 32: 499–573 (1982)
14. Callan, C. G., Gross, D. J., *Phys. Rev. Lett.* 22: 156 (1969)
15. Eichten, E., et al., *Rev. Mod. Phys.* 56: 579 (1984); Altarelli, G., et al., *Nucl. Phys.* B246: 12 (1984); Halzen, F., "Top Search." *Phys. in Collision* 1987: 275 [*QCD* 161: 1542 (1987)]; Albajar,